The Pennsylvania State University

The Graduate School

Eberly College of Science

SYNTHESIS AND APPLICATIONS OF GOLD AND GOLD-COPPER ALLOY NANOPARTICLES

A Dissertation in

Chemistry

by

Nathan E. Motl

© 2012 Nathan E. Motl

Submitted in Partial Fulfillment

of the Requirements

for the Degree of

Doctor of Philosophy

August 2012

The dissertation of Nathan E. Motl was reviewed and approved* by the following:

Raymond E. Schaak

Professor of Chemistry

Dissertation Advisor

Chair of Committee

Thomas E. Mallouk

Evan Pugh Professor of Materials Chemistry and Physics

Lasse Jensen

Assistant Professor of Chemistry

Robert M. Rioux

Friedrich G. Helfferich Assistant Professor of Chemical Engineering

Barbara J. Garrison

Shapiro Professor of Chemistry

Head of the Department of Chemistry

*Signatures are on file in the Graduate School

Abstract

The unique physical and chemical properties of noble metal nanoparticles have enabled the materials to be utilized as invaluable tools for use in a wide range of disciplines. Many of these applications depend on the ability to intelligently modify the material shape, composition and structure. Low temperature solution methods have been shown to produce colloidally stable nanomaterials with a variety of shapes and compositions. In this dissertation I describe our recent contributions to the development and application of complex nanomaterials, specifically gold and gold-copper alloy nanoparticles.

We first demonstrate the synthesis and investigation of composition-tunable gold-copper alloy nanoparticles. This investigation was undertaken to examine the relationship between the alloy nanoparticle composition and the resulting optical properties. Specifically, highly uniform particles were examined using both powder X-ray diffraction (XRD) and energy dispersive X-ray spectroscopy (EDS). The resulting optical activity of the nanoparticles was compared with the theoretically predicted UV-Vis absorbance spectra. This study serves as a methodology template by which existing theoretical models can be tested with more complex systems.

Next we describe the novel synthesis of Au-Cu_2S hybrid nanoparticles via the phase segregation of AuCu alloy nanoparticles. Hybrid nanoparticles are characterized by discrete inorganic domains that are bound together through a solid-solid interface. These particles are often formed by nucleating the growth of a second inorganic domain on the surface of an existing particle through a seed mediated approach. As the complexity of nanomaterial synthesis and application increases, additional synthetic routes to these

materials will be required. By heating AuCu alloy nanoparticles in the presence of sulfur it was possible to phase segregate the copper component to generate Au-Cu_2S heterodimers with discrete Au and Cu_2S components. The resulting particles were examined extensively with transmission electron microscopy (TEM), energy electron loss microscopy, (EELS), XRD, EDS and UV-Vis absorbance spectroscopy. Additional control experiments were performed to support the phase segregation route to hybrid nanoparticles. This process demonstrates a new method of nanomaterial synthesis that can draw upon a vast library of alloy and intermetallic nanoparticles as precursor materials

Lastly, we demonstrate the use of both gold and copper nanoparticles for the fabrication of mesoscale components through modifying the existing lost mold – rapid infiltration forming (LM-RIF) process. Several generations of components with nano- and microscale features were shown with progressivessive improvements on part fabrication. This work served as a proof of concept, demonstrating a general technique that could incorporate the vast array of metal nanoparticles available into part fabrication. In addition to the miniaturization of existing components, this process could potentially lead to such medical advances as microsurgical instruments and localized drug delivery.

.

Table of Contents

List of Figures

List of Tables

List of Abbreviations

CAAM	Chemically aided attrition milling
CIP	Cold isostatically pressed
CTAB	Cetyltrimethylammonium Bromide
EDS	Energy dispersive X-ray spectroscopy
EELS	Energy electron loss spectroscopy
fcc	Face centered cubic
FFT	Fast Fourier transform
HRTEM	High resolution transmission electron microscope
ksi	Kilopound per square inch
LM-RIF	Lost mold – rapid infiltration forming
NIR	Near infrared
NMR	Nuclear magnetic resonance
PDDA	poly(diallyldimethylammonium chloride)
PVP	Poly(vinylpyrrolidone)
RIF	Rapid infiltration forming
rpm	Rotations per minute

STEM	Scanning transmission electron microscope
TEM	Transmission electron microscope
UV-Vis	Ultraviolet-visible
XRD	X-ray diffraction

Acknowledgements

I would first like to thank God for granting me the grace to thrive in graduate school. I could not have completed the work presented within this dissertation without Him. Much love to my wife Laura Motl for all of her care and support throughout my graduate studies. You are my sunshine, thank you for being the anchor and source of light in my solar system.

I would like to thank my research advisor, Dr. Raymond E. Schaak for all of his guidance and providing an intellectually encouraging research environment for my scientific endeavors at the Pennsylvania State University. I would also like to thank the members of my graduate committee: Dr. Thomas E. Mallouk, Dr. Lasse Jensen, and Dr. Robert M. Rioux for their time spent in ensuring that I meet the requirements of a doctoral degree. I would also like to thank my collaborators Dr. James H. Adair, Dr. Lasse Jensen, Dr. Nicholas E. Antolino, Ebo Ewusi-Annan, and Christopher Leh for bringing their knowledge and expertise to projects that I could not have completed on my own.

Thanks and appreciation to past and present members of the Schaak group, especially Danielle DeCicco, Bobby Laraway, Phil Sabato, P.J. Rosenstock, Dr. James F. Bondi, Dr. Ian T. Sines, Dr. Su-Il In, and Eric J. Popczun for all of their assistance with material synthesis and characterization as well as many hours of thoughtful discussion. I would like to thank Dr. Jeffrey Pyun for first introducing me to nanoparticle synthesis, Dr. Michael Shaw for guiding my early steps into the wonderful world of synthetic chemistry, and Dr. Rebecca Lindell for encouraging my academic development.

Special thanks to Jeff Crisman for getting me to relax now and then, David Cacace for his perspectives and discussions, and Josh Antoline for reminding me that badgers don't shrug. I would also like to thank my family for all of their support. Specifically my parents, Edward and Kimberly Motl, for doing everything they could to encourage me when I told them as a small child that I wanted to be a scientist when I grow up. I would also like to thank my sister Nicole Motl for showing me that a little sibling rivalry can be a good thing.

Chapter I

Introduction

1.1 Noble Metal Nanoparticles

In recent years, much attention has been given to the development of colloidal nanoparticle applications. By incorporating principles from traditionally disparate fields such as materials science and biology, it has become possible to generate a wide variety of complex nanomaterials. The unique properties that result from these materials have been utilized to solve problems in a plethora of disciplines ranging from solar energy conversion[1] and catalysis[2] to biomedicine[3] and agriculture.[4]

Of particular interest are noble metal nanoparticles. The unique physical and chemical properties that these materials possess have made them invaluable tools in the development and application of advanced nanomaterials. When the dimensions of noble metal particles are reduced into the nanometer regime, the materials can exhibit properties that are unique from their bulk counterparts due to such effects as quantum confinement[5] and increased surface area. For example, decreasing the size of the particles into the nanoscale greatly increases the exposed surface area of the material, often resulting in a dramatic increase in the chemical reactivity of the surface. This phenomenon has been especially useful in catalysis, where the use of platinum[6] and palladium[7] nanoparticles has shown a dramatic improvement in catalytic activity over their bulk counterparts. Additionally, changes in the geometry of noble metal nanoparticles can also have a profound impact on the catalytic and chemical reactivity of the nanoparticle surface.[8] By inducing preferential generation of specific crystal planes through anisotropic particle formation, it is possible to improve the reactivity of the

material. Platinum nanowires, for example, have been shown to have higher catalytic activity than platinum spheres due to the increased exposure of the (110) crystal planes.[9]

Also of particular interest are the optical properties that emerge from the collective oscillation of the surface electrons in noble metal nanoparticles.[10] This collective oscillation is often referred to as a localized surface plasmon and results in a characteristic absorbance band, typically in the ultraviolet and visible region of the electromagnetic spectrum. This plasmonic resonance makes metallic nanoparticles suitable for a wide variety of applications in areas such as miniaturized optical devices, photonic circuitry, biological imaging, and optically targeted drug delivery.[11-14] By altering the structure and geometry of these nanomaterials, it is possible to change the frequency at which the surface electrons oscillate.[15] This phenomenon has been extensively studied in gold nanoparticle systems where a wide variety of shapes and sizes are readily accessible.[16] Gold nanoshells, for example, can be prepared with a variable shell thickness.[17] The resulting plasmon band of the material can then be red-shifted by either increasing the shell diameter, or decreasing the shell thickness. As the application of these materials begin to require more sophisticated control of the nanomaterial properties, the synthetic techniques employed in the generation of these materials will require more precise control over the resulting size, composition, and morphology.

The methods utilized to synthesize these materials can be generally classified as "top-down" or "bottom-up" approaches. In top-down approaches, a bulk material is reduced to the nanoscale though a high energy process. Examples of such a process include ball-milling,[18] laser ablation,[19] or explosive detonation.[20] These methods typically

involve complex experimental setups, harsh reaction conditions, and typically do not provide much control in the final material yield and morphology. In the alternative bottom-up approaches, nanoparticles are generated by nucleation from atomic or molecular precursors and subsequently grown into the desired nanoparticles. Examples of such techniques include flame spray synthesis,[21] chemical vapor deposition,[22] the sol-gel process,[23] and other solution based methods.

These approaches typically result in a high degree of control over particle morphology and composition due to the relatively low temperatures and the ability to precisely tune the particle growth through precursor concentration, reducing agents, molecular and polymeric surface stabilizers, and other reagents. These additives allow for surface modification which can result in colloidal stability and application of the nanoparticles in both polar and non-polar media. Solution methods also enable the use of surface stabilizers which can facilitate more control over the growth direction and surface chemistry of the resulting nanoparticles.[15] Solution based synthesis of nanoparticles has been shown to be sensitive to minute alteration in reagent concentration, often resulting in drastic differences in particle morphology. For example, it has recently been shown that small changes in trace halide concentration can make the difference between spheres, rods, and plates in aqueous gold nanoparticle synthesis.[24] This sensitivity combined with the amounts of solvent used, often makes large scale production of these materials difficult through solution methods.

Despite these disadvantages, solution methods have provided a diverse library of tunable sizes and morphologies for a variety of materials including metal oxides, chalcogenides, and noble metals. Solution methods have also been shown to generate

complex nanostructures, such as core-shell[25] nanoparticles where one inorganic material completely encapsulates another, and heterodimer and oligomer type hybrid nanoparticles[26-27] that contain discrete inorganic domains connected by a solid-state interface. These advanced materials provide a wider range of applications for noble metal nanoparticles by incorporating the functionality of multiple inorganic substances containing various compositions and morphologies within the same nanoscale material.

1.1 Gold Nanoparticles

Gold nanoparticles are one of the earliest examples of colloidally stable nanoparticles and are widely used for their strong optical properties.[28] It is possible to generate colored glass for example, by adding finely processed gold to glass.[29] The vibrant red-wine colors that result were attributed first by Faraday to be the result of the small size of the particulate gold.[30] This color is the result of the surface plasmon resonance of the material and is subsequently dependent on the particle morphology. Spherical gold nanoparticles, for example, can possess a plasmon band typically ranging from 520 nm to the infrared regime depending on the particle size and shape.[31] This optical activity, combined with the biocompatibility of gold, have allowed for these materials to be used in genetic manipulation,[32] anti-cancer therapy,[13] and medical imaging.[33] The low temperatures used in solution methods, and the variety of polymeric and molecular stabilizers for which gold nanoparticles have an affinity, has allowed for a wide variety of sizes and shapes to be accessed. The library of shapes that has been demonstrated thus far includes spheres, rods, plates, wires, ribbons, octahedral, and shells

in addition to many others.[34] These shapes have enabled diverse applications such as data storage,[35] enhanced spectroscopy,[36] and optical circuitry.[37]

Many of the applications of these materials depend on the ability to intelligently modify the optical properties.[28,33] One method of altering the surface plasmon of gold nanoparticles is to alter the morphology of these materials. For example, aqueous gold nanoparticles can be synthesized with progressively increasing aspect ratios.[38] This results in a progressive redshift in the plasmon band, resulting in tunability from the visible into the infrared.

The optical properties of gold nanoparticles have also been modified by alloying the particle with another metal. The resulting plasmon band behaves as a hybrid of the two materials, and possesses variability based upon the proportion incorporated. Gold has been previously shown to form alloy nanoparticles with other optically active materials such as copper and silver.[39] This ability to tune material properties *via* composition, combined with the wide variety of shapes available makes gold nanoparticles an attractive platform from which to develop further advances in nanomaterial design and synthesis.

1.3 Alloy Nanoparticles

Many of the current applications of noble metal nanoparticles depend on the ability to intelligently control the properties of the material. One method of exercising such control is through changing the composition of the nanoparticle *via* the formation of alloys and intermetallic compounds. Alloys can be described as a mixture of two or more elements in which the resulting crystal structure is identical to the crystal structure of the

constituent elements. These materials behave as a solid solution in which the composition can typically exist over a wide range of compositions without compromising the original crystal structure. Intermetallic compounds, however, occur when the resulting crystal structure is different from that of the constituent elements. These materials can be highly ordered and typically exist over a narrower composition range than their alloy counterparts.

When these materials are incorporated into nanoparticle systems, synergistic effects in addition to property tunability can be observed. Alloy nanoparticles comprised of nickel and palladium, for example, have been shown to synergistically enhance the catalysis of coupling reactions. The resulting catalytic activity of the alloy nanoparticles was greater than the activity of the single metal nanoparticle. These materials are traditionally generated through intimately mixing the constituent atoms together in the form of bulk powders at high temperatures over long periods of time. This process is energy intensive but necessary to ensure uniform diffusion throughout the material. When nanoparticles are used in lieu of bulk powders, the speed at which this formation occurs can be greatly increased. Since the diffusion distances are much shorter in nanoparticle systems, the formation of alloy nanoparticles can proceed at much lower temperatures with much shorter reaction times.[40] This allows for the use of solution based methods in the synthesis of alloy nanoparticles where temperatures are typically below 400°C. These low temperatures often result in the formation of non-equilibrium and metastable phases. These phases are not thermodynamically favored under the conditions present in traditional solid-state methods but often become available *via* kinetic trapping.[41]

Solution methods offer several different approaches for the synthesis of alloy and intermetallic nanoparticles. One approach involves first generating a nanoscale composite with the desired stoichiometry through either co-reduction of salt precursors or physical mixture of discrete nanoparticles, and subsequently heating the composite until the desired phase is achieved.[42] An illustration of this process is shown in figure 1.1. Although this method allows for excellent control over the product composition, the amount of sintering that occurs results in a lack of control over the particle size and shape.

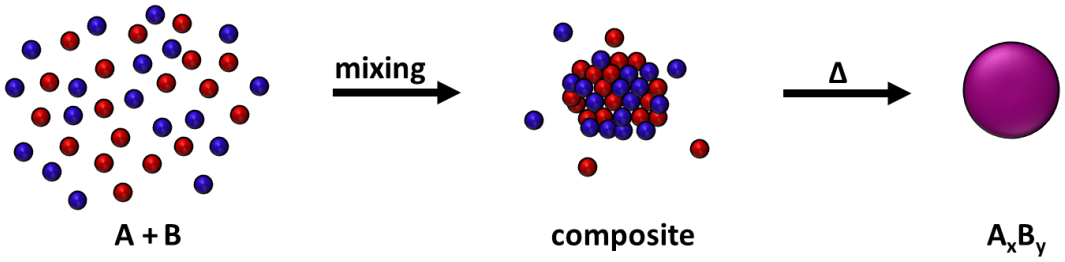

Figure 1.1 Illustration of nanoscale composite method demonstrating formation of composite *via* aggregation of preformed nanoparticles and subsequent annealing.

Another approach involves the use of premade nanoparticles as a template for conversion chemistry. In this approach, colloidally stabile nanoparticles are transformed into alloy or intermetallic compounds through chemical processes that can include diffusion,[43] ion-exchange,[44] or galvanic replacement.[45] An illustration of this process is shown in figure 1.2.

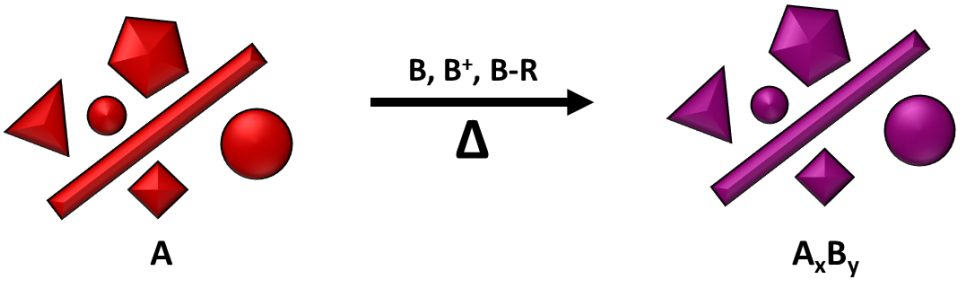

Figure 1.2 Illustration of conversion chemistry method demonstrating the conversion of preformed nanoparticles to alloy or intermetallic, while maintaining size and shape. The second metal is shown in its elemental, cationic, and organometallic forms by B, B^+, and B-R respectively.

This method has been shown to be applicable to a variety of precursors and often maintains the morphology of the original template nanoparticles. This has the benefit of allowing for compositional tunability without dramatically changing the size and shape of the material. Such tunability is invaluable in applications such as optical arrays where particle spacing is paramount and morphological variability could introduce detrimental anisotropy into the system.

An additional method involves the co-reduction of metal cations in solution to generate the desired nanoparticle.[46, 47] In this approach two or more types of metal cations are thoroughly dissolved in solution and are simultaneously reduced *via* thermal or chemical means. An illustration of this approach is shown in figure 1.3.

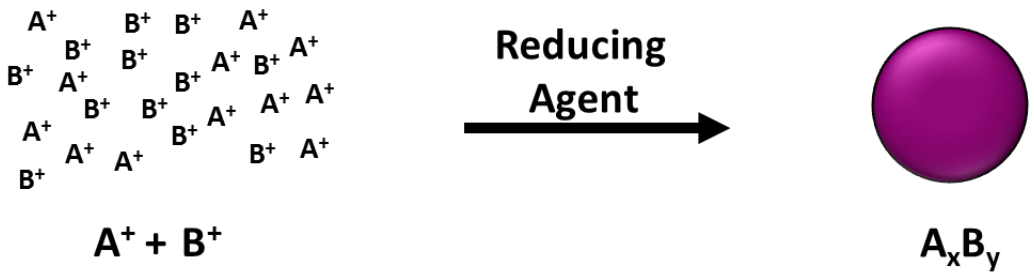

Figure 1.3 Illustration of co-reduction method demonstrating the reduction of two types of metal cations *via* a reducing agent to form an alloy or intermetallic nanoparticle.

This incorporation of surfactants and other additives into this method can often result in nanoparticle monodispersity and shape control. Although the composition of the final product can be controlled by altering the precursor ratios, this method is sensitive to changes in the reduction rate. Thus, changes in the reducing agent and temperatures used during the synthesis will often result in different nanoparticle morphologies and compositions.

These solution based routes have been used to generate composition-tunable systems involving noble metal nanoparticles. Alloy nanoparticles containing gold and silver for example have been prepared in aqueous solution through a solution based co-reduction route.[48] The resulting optical properties of the material were found to vary linearly with the mole fraction of metal ions used. This composition based tuning of optical activity has also been demonstrated for a variety of gold nanoparticle based systems including gold-zinc[49] and gold-copper,[39(g)] making gold containing alloy and intermetallic nanoparticles an attractive target for composition control studies and applications.

1.4 Experimental Work

Herein is detailed the use of gold and gold alloy nanoparticles for several diverse synthetic investigations. By utilizing these versatile nanoparticles as model systems, a system of methodologies can be developed which should be applicable to similar noble metal and alloy nanoparticle systems.

In chapter II, the synthesis of composition-tunable AuCu alloy nanoparticles are investigated in order to explore the interplay between alloy nanoparticle composition and the resulting optical properties of the alloy nanoparticles. The compositions of these highly uniform particles were examined with both powder X-ray diffraction (XRD) and energy dispersive X-ray spectroscopy (EDS). The optical properties of these particles were then measured with UV-Vis spectroscopy. The experimentally determined UV-Vis spectra were then compared to spectra calculated from Mie theory using the EDS and XRD composition measurements. This study serves as a methodology template by which future plasmonic systems can be examined. By testing existing theoretical models with more complex systems, it will be possible to enhance our understanding and our ability to design specific optical properties within complex nanoparticle systems.

Chapter III examines the synthesis of Au-Cu_2S hybrid nanoparticles through a novel phase segregation mechanism. Hybrid nanoparticles are nanoparticles that are comprised of discrete inorganic domains bound to each other by a solid-state interface. These complex nanoparticles are typically formed from combining different components into a single hybrid nanoparticle; usually this process is accomplished by nucleating a second particle on the surface of an existing particle *via* a seed-mediated growth approach. As the complexity of these nanoparticle systems increases, additional synthetic

methods will be required. One novel method of generating hybrid nanostructures is through phase segregation. By heating previously synthesized AuCu alloy nanoparticles in the presence of sulfur it is possible to phase segregate the copper component in the form of Cu_2S and subsequently generate Au-Cu_2S hybrid nanoparticles. The hybrid nanoparticles are dimers with discrete Au and Cu_2S components. This demonstrates a new method of complex nanomaterial synthesis that can draw upon an increasing library of alloy and intermetallic nanoparticles as precursors.

Chapter IV details the use of colloidal gold nanoparticles for mesoscale parts through a modified version of the lost mold – rapid infiltration forming (LM-RIF) process.[50] This process, which is traditionally reserved for ceramics, involves casting concentrated nanoparticle dispersions into photolithographic masks, followed by controlled low temperature sintering and subsequent release. This microprocessing technique is ideal for producing nano- and microscale features with a wide variety of morphologies. The use of gold nanoparticles in this work serves as a test case for the incorporation of metal nanoparticles into this technique. This materials processing technique is general, capable of utilizing nanoparticles from a vast library of compositions while simultaneously combining solution based bottom-up approaches with more traditional top-down approaches. This should enable the generation of a wide range of exotic materials and for a variety of applications, particularly in the medical sciences.

1.5 References

(1) Costi, R.; Saunders, A. E.; Elmalem, E.; Salant, A.; Banin, U. *Nano Lett*. **2008**, *8*, 637.

(2) Wu, Y.; Wang, D.; Zhao, P.; Niu, Z.; Peng, Q.; Li, Y. *Inorg. Chem*. **2011,** *50*, 2046.

(3) Huang, X.; El-Sayed, I. H.; Qian, W.; El-Sayed M. A. *J. Am. Chem. Soc*. **2006** *128*, 2115.

(4) Liu, B.; Han, G.; Zhang, Z.; Liu, R.; Jiang, C.; Wang, S.; Han, M. *Anal. Chem*. **2012**, *84*, 255.

(5) Alivisatos, A.P.; *Science* **1996**, *271*, 933.

(6) Murillo, L. E.; Goda, A. M.; Chen, J. G. *J. Am. Chem. Soc*. **2007**, *129*, 7101.

(7) Roucoux, A.; Schulz, H.; Patin, H.; *Chem. Rev*. **2002**, *102*, 3757.

(8) Sau, T. K.; Rogach, A. L.; Jäckel, F.; Klar, T. A.; Feldmann, J. *Adv. Mater*. **2009**, *21*, 1.

(9) Fukuoka, A.; Higashimoto, N.; Sakamoto, Y.; Inagaki, S.; Fukushima, Y.; Ichikawa, M. *Microporous Mesoporous Mater*. **2001**, *48*, 171.

(10) Eustis, S.; El-Sayed, M. A. *Chem. Soc. Rev*. **2006**, *35*, 209.

(11) Maier, S. A.; Brongerma, M. L.; Kik, P. G.; Meltzer, S.; Requicha, A. A. G.; Atwater, A. H. *Adv. Mater.* **2001**, *13*, 1501.

(12) Mekis, A.; Chen, J. C.; Kurland, I.; Fan, S.; Villeneuve, P. R.; Joannopoulos, J. D. *Phys. Rev. Lett*. **1996**, *77*, 3787.

(13) Huang, X.; El-Sayed, I. H.; Qian, W.; El-Sayed M. A. *J. Am. Chem. Soc*. **2006** *128*, 2115.

(14) Le, F.; Brandl, D. W.; Urzhumov, Y. A.; Wang, H.; Kundu, J.; Halas, N. J.; Norlander, P. *ACS Nano*, **2008**, *2*, 707.

(15) Xia, Y.; Xiong, Y.; Lim, B.; Skrabalak, S. E. *Angew. Chem. Int. Ed*. **2008**, *47*, 2.

(16) (a) Lim, B.; Camargo, P. H. C.; Xia, Y. *Langmuir*, **2008**, *24*, 10437. (b) Li, C.; Shuford, K. L.; Chen, M.; Lee, E. J.; Cho, S. O. *ACS Nano*, **2008,** *2*, 1760. (c) Sanjanlal, P. R.; Sreeprasad, T. S.; Nair, A. S.; Pradeep, T. *Langmuir*, **2008**, *24*, 4607. (d) Chu, H. C.; Kuo, C. H.; Huang, M. H. *Inorg. Chem*. **2006**, *45*, 808. (e) Millstone, J. E.; Wei, W.; Jones, M. R.; Yoo, H. Mirkin, C. A. *Nano Lett*. **2008**, *8*, 2526. (f) Bardhan, R.; Neuman, O.; Mirin, N.; Wang, H.; Halas, N. J. *ACS Nano* **2009**, *3*, 266. (g) Bakr, O. M.; Wunsch, B. H.; Stellacci, F. *Chem. Mater*. **2006**, *18*, 3297.

(17) Schwartzburg, A. M.; Olson, T. Y.; Talley, C. E.; Zhang, J. Z. *J. Phys. Chem. B* **2006**, *110*, 19935.

(18) Ding, C.; Jihua, C.; Hongge, Y.; Zhenhua, C. *Mater. Sci. Eng. A* **2007**, *444*, 1.

(19) Pithawalla, Y. B.; El-Shall, M. S.; Deevi, S. *Scripta Mater.* **2003**, *48*, 671.

(20) Kang, B. Y.; Ryoo, H. S.; Hwang, W.; Hwang, S. K.; Kim, S. W. *Mater. Sci. Eng., A* **1999**, *270*, 330.

(21) Hampdensmith, M. J.; Kodas, T. T. *Chem. Vapor Depos.* **1995**, *1*, 8.

(22) Athanassiou, E. K.; Grass, R. N.; Stark, W. J. *Aerosol Sci. Technol.* **2010**, *44*, 161.

(23) Wright, J. D.; Sommerdijk, A. J. M. *Sol-Gel Materials: Chemistry andApplications*, Gordon and Breach: Amsterdam, 2001.

(24) Smith, D. K.; Korgel, B. A. *Langmuir* **2008**, *24*, 644.

(25) Lu, W.; Wang, B.; Zeng, J.; Wang, X.; Zhang, S.; Hou, J. G. *Langmuir*, **2005**, *21*, 3684.

(26) Shi, W.; Zeng, H.; Sahoo, Y.; Ohulchanskyy, T. Y.; Ding, Y.; Wang, Z. L.; Swihart, M.; Prasad, P. N. *Nano Lett*. **2006**, *6*, 875.

(27) Buck, M. R.; Bondi, J. F.; Schaak, R. E. *Nat. Chem*. **2012**, *4*, 37.

(28) Odom, T. W.; Nehl, C. L. *ACS Nano* **2008,** *2*, 612.

(29) Daniel, M. C.; Astruc, D. Chem. Rev. **2004**, *104*, 293.

(30) Edwards, P. P.; Thomas, J. M. *Angew. Chem. Int. Ed*. **2007**, *46*, 5480.

(31) Jana, N. R.; Gearheart, L.; Murphy, C. J. *J. Phys Chem. B* **2001,** *105*, 4065.

(32) Csaki, A.; Garwe, F.; Steinbruck, A.; Maubach, G. F.; Weise, A.; Riemann, I.; Konig, K.; Fritzsche, W. *Nano Lett*. **2007**, *7*, 247.

(33) Loo, C.; Lowery, A.; Halas, N.; West, J. *Nano Lett*. **2005**, *5*, 709.

(34) (a) Xue, C.; Milstone, J. E.; Li, S.; Mirkin, C. A. *Angew. Chem. Int. Ed.* **2007**, *46*, 8436. (b) Li, C.; Shuford, K. L.; Chen, M.; Lee, E. J.; Cho, S. O. *ACS Nano*, **2008,** *2*, 1760. (c) Chu, H. C.; Kuo, C. H.; Huang, M. H. *Inorg. Chem*. **2006**, *45*, 808. (d) Link, S.; El-Sayed, M. A. *J. Phys. Chem. B* **1999**, *103*, 4212. (e) Khanal, B. P.; Zubarev, E. R. *J. Am. Chem. Soc*. **2008**, *130*, 12634. (f) Kim, F.; Sohn, K.; Wu, J.; Huang, J. *J. Am Chem Soc*. **2008**, *130*, 14442. (g) Ha, T. H.; Koo, H. J.; Chung, B. H. *J. Phys. Chem. C* **2007,** *111*, 1123. (h) Millstone, J. E.; Wei, W.; Jones, M. R.; Yoo, H. Mirkin, C. A. *Nano Lett*. **2008**, *8*, 2526. (i) Novo, C.; Mulaney, P. *Nano Lett*. **2007**, *7*, 520. (j) Tiwari, N.; Kalele, S.; Kulkarni, S. K. *Plasmonics*, **2007**, *2*, 231. (k) Lim, B.; Camaro, P. H. C.; Xia, Y. *Langmuir*, **2008**, *24*, 10437. (l) Xie, J.; Lee, J. Y.; Wang, D. I. C. *J. Phys. Chem. C* **2007**, *111*, 10226. (m) Sanjanlal, P.

R.; Sreeprasad, T. S.; Nair, A. S.; Pradeep, T. *Langmuir*, **2008**, *24*, 4607. (n) Wang, H.; Halas, N. J. *Adv. Mater*. **2008**, *20*, 820.

(35) Wan, D.; Chen, H.; Tseng, S.; Wang, L. A.; Chen, Y. *ACS Nano* **2010,** *4,* 165.

(36) Le, F.; Brandl, D. W.; Urzhumov, Y. A.; Wang, H.; Kundu, J.; Halas, N. J.; Norlander, P. *ACS Nano*, **2008**, *2*, 707.

(37) Chon, J. W. M.; Bullen, C.; Zijlstra, P.; Gu, M. *Adv. Funct. Mater*. **2007**, *17*, 875.

(38) Nikoobakht, B.; El-Sayed, M. A. *Chem. Mater*. **2003**, *15*, 1957.

(39) (a) Wang, C.; Peng, S.; Chan, R.; Sun, S. *Small* **2009**, *5*, 56. (b) Mallin, M. P.; Murphy, C. J.; *Nano Lett.* **2002**, *2*, 1235. (c) Radziuk, D. V.; Zhang, W.; Schukin, D.; Möhwald, H. *Small* **2010**, *6*, 545. (d) Bok, H. M.; Shuford, K. L.; Kim, S.; Kim, S. K.; Park, S. *Langmuir* **2009**, *25*, 5266. (e) Kim, M. J. ; Na, H. J.; Lee, K. C.; Yoo, E. A.; Lee, M. *J. Mater. Chem*. **2003**, *13*, 1789. (f) Pal, U.; Sanchez-Ramirez, J. F.; Liu, H. B.; Medina, A.; Ascencio, J. A. *Appl. Phys. A* **2004**, *79*, 79. (g) Sra, A. K.; Schaak, R. E. *J. Am. Chem. Soc.* **2004**, *126*, 6667. (h) Chen, W.; Yu, R.; Li, L.; Wang, A.; Peng, Q.; Li, Y. *Angew. Chem. Int. Ed*. **2010**, *122*, 2979. (i) Henkel, A.; Jakab, A.; Brunklaus, G.; Sönnichsen, C. *J. Phys Chem C* **2009**, *113*, 2200.

(40) Zeng, D.; Hampden-Smith, M. J. *Chem. Mater.* **1992**, *4*, 968.

(41) Williams, J. R.; Johnson, D. C. *Inorg. Chem.* **2002**, *41*, 4127.

(42) Schaak, R. E.; Sra, A. K.; Leonard, B. M.; Cable, R. E.; Bauer, J. C.; Han, Y. F.; Means, J.; Teizer, W.; Vasquez, Y.; Funck, E. S. *J. Amer. Chem. Soc.* **2005**, *127*, 3506.

(43) Yin, Y.; Erdonmez, C. K.; Cabot, A.; Hughes, S.; Alivisatos, A. P. *Adv. Funct. Mater*. **2006**, *16*, 1389.

(44) Son, D.H.; Hughes, S.M.; Yin, Y.; Alivisatos, A.P. *Science* **2004**, *306*, 1009.

(45) Vasquez, Y.; Sra, A. K.; Schaak, R. E. *J. Am. Chem. Soc.* **2005**, *127*, 2504.

(46) Liu, Q.; Yan, Z.; Henderson, N. L.; Bauer, J. C.; Goodman, D. W.; Batteas, J. D.; Schaak, R. E. *J. Am. Chem. Soc*. **2009**, *131*, 5720.

(47) Pal, U.; Sanchez-Ramirez, J. F.; Liu, H. B.; Medina, A.; Ascencio, J. A. *Appl. Phys. A* **2004**, *79*, 79.

(48) Link, S.; Wang, Z. L.; El-Sayed, M. A. *J. Phys. Chem. B* **1999**, *103*, 3529.

(49) Schaefer, Z. L.; Vaughn II, D. D.; Schaak, R. E. *J. Alloys Compd.* **2010**, *490*, 98.

(50) (a) Antolino, N. E.; Hayes, G.; Kirkpatrick, R.; Muhlstien, C. L.; Frecker, M. I.; Mockensturm, E. M.; Adair, J. H. *J. Am. Ceram. Soc*. **2009**, *92*, S63. (b) Antolino, N. E.; Hayes, G.; Kirkpatrick, R.; Muhlstien, C. L.; Frecker, M. I.; Mockensturm, E. M.; Adair, J. H. *J. Am. Ceram. Soc*. **2009**, *92*, S70.

Chapter II

Au-Cu Alloy Nanoparticles with Tunable Compositions and Plasmonic Properties: Experimental Determination of Composition and Correlation with Theory

2.1 Introduction

The unique and tunable optical properties of plasmonic nanoparticles have made them attractive targets for a wide range of applications that include communications,[1,2] alternative energy,[3,4] molecular sensing,[5,6] and spectroscopy,[7-9] as well as medical imaging,[10] detection,[11,12] and therapy.[12,13] Such diverse applications require the ability to precisely tune the plasmonic properties,[14,15] which depend sensitively on particle morphology[16-18] and are often tuned *via* nanoparticle shape and size.[19] This approach is common for metals such as gold [20] and silver,[21,22] for which a wide range of sizes and shapes are readily accessible. The plasmonic properties can also be tuned by changing the composition.[23] For example, the resonance frequency of gold can be blue-shifted by alloying with silver [24,26] and red-shifted by alloying with copper.[26-30]

In recent years, there have been several reports describing composition-tunable plasmonic properties of colloidal metal alloy nanoparticle systems. For example, El-Sayed and co-workers reported tunable plasmon resonance frequencies in colloidal Au-Ag alloy nanoparticles made using a citrate reduction route.[18] More recently, Sönnichsen

---

[*] Reproduced in part with permission from J. Phys. Chem. C 114, N.E. Motl, E. Ewusi-Annan, I.T. Sines, L. Jensen, R.E. Schaak, Au-Cu Alloy Nanoparticles with Tunable Compositions and Plasmonic Properties: Experimental Determination of Composition and Correlation with Theory, 19263-19269, Copyright 2010 American Chemical Society.

and co-workers reported tunable plasmonic properties in colloidal Au-Cu nanorods synthesized using a seed-mediated growth strategy.[30] Our group has shown tunable plasmon resonance frequencies in colloidal Au-Cu [28] and Au-Zn nanoparticles.[31]

Theoretical modeling and experimental characterization are both central to the ability to predictably synthesize and use these colloidal metal alloy nanoparticles with tunable compositions and plasmonic properties. The theory describing the plasmonic properties of metal nanoparticles – including the resonance frequencies, line widths, and profile shapes – is well established.[32,33] While modeling the optical properties of pure metal nanoparticles is straightforward, it is more complicated to model metal alloys since the dielectric constant is rarely available. Therefore, to describe the optical properties of metal alloys one typically relies on a simple linear combination of the dielectric constants of the constituent free metals.[18,34] Robust systems for experimentally testing the validity of this linear combination model, however, are rare.

From an experimental perspective, several techniques have been applied to the compositional characterization of plasmonic alloy nanoparticles, including X-ray photoelectron spectroscopy,[26] solid-state NMR,[30] and electron diffraction.[30] Two of the most common techniques, however, are energy dispersive X-ray spectroscopy (EDS) [29] and powder X-ray diffraction (XRD).[30] EDS is usually best classified as a semi-quantitative technique for composition analysis unless careful standards are used, and extraneous signals attributable to sample holders are sometimes observed. XRD can provide estimates of alloy composition by analyzing the peak positions according to Vegard's law.[35] However, colloidal nanoparticle samples are not always large enough, or easily isolated in powder form, to facilitate powder XRD analysis. In some cases, e.g.

Au-Ag alloys, nearly identical lattice constants preclude composition analysis by XRD. Consequently, literature reports sometimes do not include detailed experimental composition analyses for plasmonic alloy nanoparticles, instead inferring the composition from the plasmon resonance frequency that is derived from theoretical modeling.[18]

With these factors in mind, a disconnect exists between theoretical prediction of plasmon resonance frequencies for a particular alloy composition and accurate experimental validation of that composition in the colloidal nanoparticles. The Au-Cu system provides an ideal platform for such studies. Based on the phase diagram,[36] Au and Cu form a complete solid solution, which facilitates a high degree of composition tunability for $Au_{1-x}Cu_x$ alloys. As colloidal nanoparticles, composition-tunable Au-Cu alloys have been made using several methods, including the polyol process,[37] seed-mediated growth,[30] and borohydride co-reduction.[27] For example, Sönnichsen and co-workers synthesized Au-Cu alloy nanorods using a seed-mediated growth strategy.[30] Li and co-workers used a seed-mediated diffusion route to form AuCu and $AuCu_3$ nanoparticles.[29] Previously, the Schaak group has described a polyol route to AuCu and $AuCu_3$ nanoparticles.[37]

In this chapter, the synthesis of a series of colloidal $Au_{1-x}Cu_x$ alloy nanoparticles with compositions that are tunable from $x = 0$ to 0.5 is described. The particles are highly uniform in both shape and size, providing high-quality spherical particles for which theoretical modeling of the plasmonic properties is possible. The compositions of these alloy nanoparticles are independently determined by both EDS and XRD, as are the errors associated with each of the measurements. The experimentally determined absorption spectra for each sample are compared with theoretically predicted spectra

based on the compositions determined by both EDS and XRD. This provides an in-depth analysis of the interplay between composition and plasmon resonance frequencies based on both experiment and theory. The results show that, overall, EDS and XRD data are both acceptable for estimating composition and the corresponding plasmon resonance frequencies. However, for $Au_{1-x}Cu_x$, the XRD data are more accurate at smaller values of *x* and the EDS data are more accurate for larger values of *x*. Additionally, for the Au-Cu system, discrepancies between the experimentally determined plasmon resonance frequencies and those predicted by theory are found, which suggests inaccuracies in using a simple linear mixing rule to determine the dielectric constant of these alloys.

2.2 Experimental Details

2.2.1 Materials Used

Hydrogen tetrachloroaurate trihydrate [99.99%, $HAuCl_4 \cdot 3H_2O$], 1-octadecene [tech. 90%, $C_{18}H_{36}$], sodium borohydride [98% $NaBH_4$], cetyltrimethylammonium bromide [98% $((C_{16}H_{33})N(CH_3)_3)Br$], ascorbic acid [99% $C_6H_8O_6$], indium chloride [anhydrous 99.99% $InCl_3$], and oleic acid [tech. 90%, $C_{18}H_{34}O_2$] were purchased from Alfa-Aesar. 1,2-Hexadecanediol [tech. 90%, $C_{16}H_{34}O_2$], copper (II) acetylacetonate [99.99%, $Cu(OOCCH_3)_2 \cdot H_2O$], poly(diallyldimethylammonium chloride) [35 wt% in H_2O M_W < 100,000], and oleylamine [tech 70%, $C_{18}H_{37}N$] were purchased from Sigma Aldrich. 1-Octadecene, oleic acid and oleylamine were transferred into the glovebox using a freeze-thaw degassing method. All glassware was dried in an oven at 120°C before use in the govebox, and all reactions were carried out on a Schlenk line using standard air-free techniques unless otherwise noted.

2.2.2 Synthesis of Au-Cu Alloy Nanoparticles

In a typical synthesis (sample "d" in the figure 2.1 and table 2.1), 45 mg of $HAuCl_4 \cdot 3H_2O$, 28 mg of $Cu(acac)_2$, and 100 mg of 1,2-hexadecanediol were weighed in an Ar-filled glovebox and placed inside a 100-mL round bottom flask along with 600 µL of oleylamine, 800 µL of oleic acid and 5 mL of 1-octadecene. After the reaction vessel was sealed and removed from the glovebox, the solution was stirred vigorously at room temperature for 90 min to ensure dissolution and then heated to 120°C over the course of 30 min. Sonication of the metal salts is avoided, as it results in particle polydispersity. The solution was further heated to 225°C over the course of 30 min and was subsequently allowed to cool to room temperature. The product was precipitated using a 3:1 mixture of acetone and hexanes and then centrifuged at 12,000 rpm for 10 min. The precipitate was then dispersed in a solution of 1% oleylamine and 1% oleic acid in hexanes and then centrifuged at 3,000 rpm for 5 min to remove any larger particles or aggregates. The product in the supernatant was precipitated by adding an equivalent volume of ethanol, centrifuged at 12,000 rpm for 10 min, and then dispersed in hexanes.

Other $Au_{1-x}Cu_x$ nanoparticle samples with different Au:Cu ratios were prepared by changing the molar ratio of $HAuCl_4 \cdot 3H_2O$: $Cu(acac)_2$ in the range of 43-47 mg of $HAuCl_4 \cdot 3H_2O$ and 27-109 mg of $Cu(acac)_2$ while all other concentrations, amounts, and conditions remained unchanged. This composition tunability through the modification of the precursor ratios is not precisely stoichiometric. Although an increase in the copper precursor will generally result in an increase in the copper content of the resulting material, the exact compositions of the nanoparticles are not entirely predictable based

upon the metal concentration ratios. To prepare gold nanoparticles without copper, the reaction solution was cooled after heating to 120°C rather than heating to 225°C.

2.2.3 Characterization

Powder X-ray diffraction (XRD) patterns were obtained at room temperature using a Bruker-AXS D8 Advance diffractometer with Cu Kα radiation and a LynxEye 1-D detector. Refined lattice constants were obtained using Chekcell.

UV-Visible absorption spectra were collected using an Ocean Optics HR4000 spectrometer with a Micropack DH-2000 BAL UV-Vis NIR light source. Nanoparticle samples were dispersed in hexanes for UV-Vis data collection.

Transmission electron microscopy (TEM) images were obtained using a JEOL 1200 EX-II microscope operating at an accelerating voltage of 80 kV. Samples for TEM analysis were prepared by drop-casting hexane-dispersed nanoparticles onto nickel TEM grids. Energy dispersive X-ray spectroscopy (EDS) data were acquired using a FEI Quanta 200 environmental scanning electron microscope operating in high vacuum mode.

2.2.4 Computational Details

The absorption spectra of the nanoparticles were simulated using Mie theory.[33] The dielectric constants for Au and Cu were taken from Johnson and Christy[38], and the dielectric constant of the surrounding medium (hexane) was taken to be $\varepsilon_m = 1.77$. The size of the nanoparticles was taken as the experimentally determined average diameters reported in the text. Since the particle sizes are generally below 10 nm, size corrections

were included in the dielectric constants to account for additional surface scattering effects due to a decreased electron mean free path as [39]

$$\varepsilon(R,\omega) = \varepsilon_{bulk}(\omega) + \frac{\omega_p^2}{\omega^2 + i\omega\gamma} - \frac{\omega_p^2}{\omega^2 + i\omega(\gamma + \frac{\upsilon_F}{R})}$$

where $\varepsilon_{bulk}(\omega)$ is the bulk dielectric constant for the metal, ω_p the bulk plasmon frequency (Au: 8.89 eV, Cu: 8.76 eV), γ is the collision frequency (Au: 0.07088 eV, Cu: 0.0955 eV), υ_F is the Fermi velocity (Au: 1.4×10^6 m/s, Cu 1.57×10^6 m/s), and R is the radius of the nanoparticle. For the $Au_{1-x}Cu_x$ alloys a simple linear combination of the dielectric constants was used as $\varepsilon(R,\omega) = (1-x)\,\varepsilon_{Au}(R,\omega) + x\varepsilon_{Cu}(R,\omega)$.

2.2.5 Acknowledgement of Author Contributions

Nathan Motl, Ebo Ewusi-Annan, and Ian Sines contributed to work presented in this chapter. Nathan Motl synthesized the alloy nanoparticles, and collected the XRD, TEM and UV-Vis characterization data. EDS measurements were taken by Ian Sines. Simulation of the absorbance spectra was performed by Ebo Ewusi-Annan. Refined lattice constants were obtained using Chekcell as performed by Nathan Motl. Gold nanorods were synthesized by Nathan Motl, Phil Sabato, P.J. Rosenstock, Bobby Laraway, and Danielle DeCicco. In_2Au nanoparticles were synthesized by Nathan Motl.

2.3 Results and Discussion

2.3.1 Transmission Electron Microscopy

Monodisperse spherical nanoparticles of $Au_{1-x}Cu_x$ alloys were synthesized by modifying a method previously used to make CuPt nanoparticles.[40] Figure 2.1 shows

TEM images for eight samples of $Au_{1-x}Cu_x$ alloy nanoparticles synthesized by varying the ratio of $Cu(acac)_2$: $HAuCl_4 \cdot 3H_2O$ while all other experimental details (reagents, concentrations, temperatures, and times) remained unchanged.

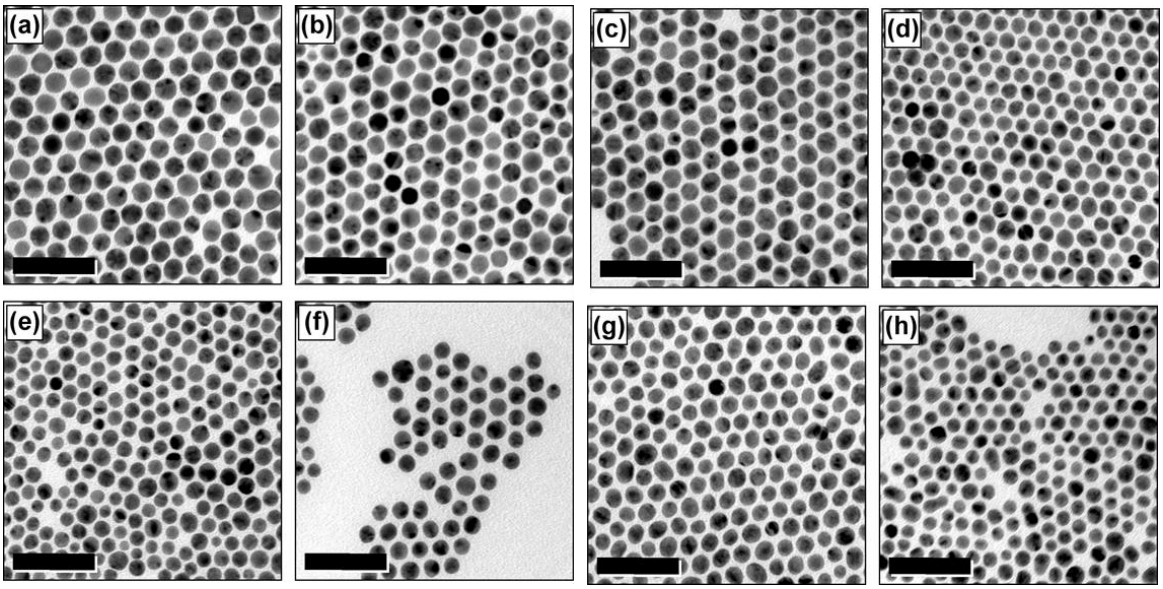

Figure 2.1 Representative TEM images for all of the $Au_{1-x}Cu_x$ nanoparticle samples. Sample (a) is pure Au, and samples (b) through (h) have increasing amounts of Cu. All scale bars are 50 nm.

The TEM images indicate that the $Au_{1-x}Cu_x$ nanoparticles are spherical and relatively monodisperse, and this is confirmed by the additional TEM images and size distribution histograms included in figures 2.2 and 2.3. In general, the peaks in the size distribution histograms indicate average particle diameters of 8–13 nm, with all samples having standard deviations of 1–2 nm. Statistical data for each sample are collected in table 2.1.

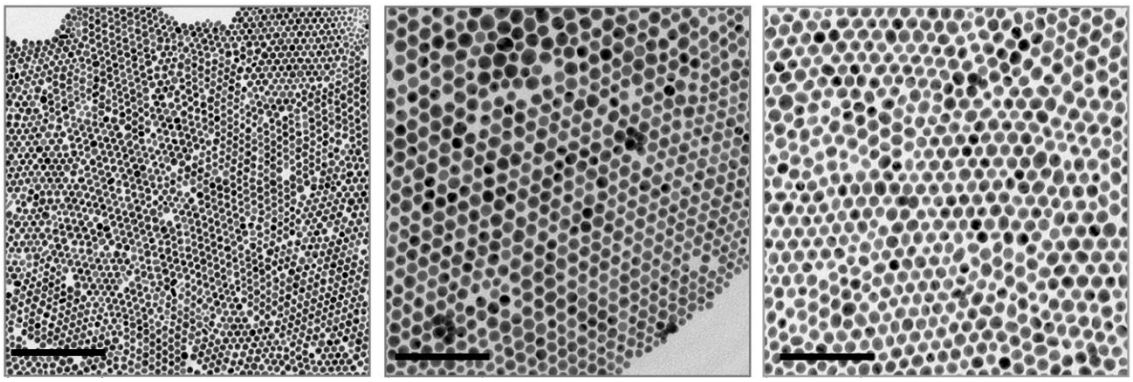

Figure 2.2 Additional larger-area TEM images for samples (left to right) a (scale bar 200 nm), d, and g (scale bars 100 nm), based on the sample designation used in figure 2.1.

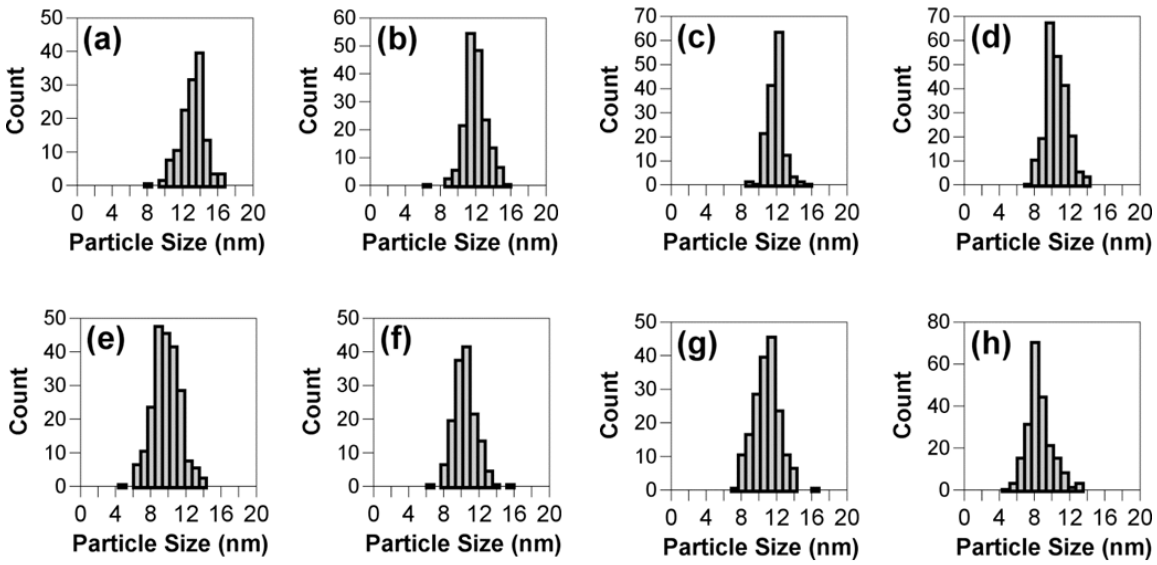

Figure 2.3 Size distribution histograms for the $Au_{1-x}Cu_x$ nanoparticles shown in figure 2.1

Sample	Size (nm)	Lattice Constant (Å)	Composition (x in $Au_{1-x}Cu_x$) by XRD (Vegard's Law)	Composition (x in $Au_{1-x}Cu_x$) by EDS	Plasmon Resonance Frequency (nm)
a	13 ± 1	4.077(3)	0.00	0.00 ± 0.07	523
b	12 ± 1	4.054(4)	0.04	0.15 ± 0.03	525
c	12 ± 1	4.058(4)	0.03	0.18 ± 0.04	523
d	10 ± 1	4.048(6)	0.05	0.18 ± 0.04	525
e	10 ± 2	4.033(6)	0.08	0.19 ± 0.02	533
f	10 ± 1	4.027(3)	0.10	0.21 ± 0.05	528
g	11 ± 1	3.98(2)	0.20	0.35 ± 0.02	525
h	8 ± 1	3.88(2)	0.41	0.48 ± 0.01	545

Table 2.1 Sizes, lattice constants, compositions determined by XRD and EDS, and plasmon resonance frequencies for all $Au_{1-x}Cu_x$ nanoparticle samples.

2.3.2 Powder X-Ray Diffraction

Figure 2.4 shows powder XRD data for all of the $Au_{1-x}Cu_x$ samples. The XRD patterns in figure 2.4a are consistent with single-phase fcc alloys with no observable impurities of CuO_x or phase-segregated metals. Figure 2.4b shows the XRD patterns enlarged to highlight only the (111) and (200) reflections. As more Cu is incorporated into the $Au_{1-x}Cu_x$ samples, the peaks clearly shift to the right. This shift is consistent with the alloying of Au and Cu. For the samples with higher Cu content, slight peak asymmetry could suggest a range of alloy compositions in the samples. Refined lattice constants and associated standard deviations (table 2.1) were obtained for each sample using the XRD data.

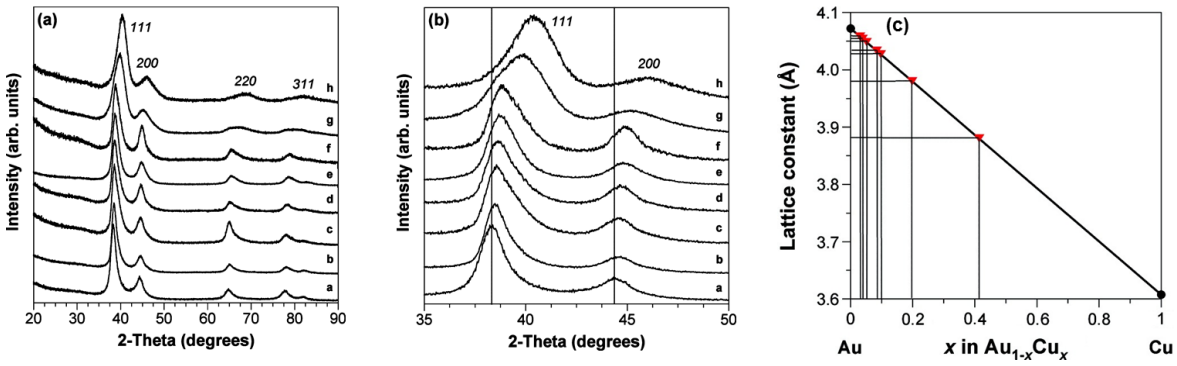

Figure 2.4 Powder XRD data for all $Au_{1-x}Cu_x$ nanoparticle samples. Full diffraction patterns are presented in (a), and the zoomed-in regions showing the (111) and (200) reflections are presented in (b). The vertical lines in (b) correspond to the (111) and (200) peak positions for Au. Vegard's law plot (c) of lattice constant vs. composition for all $Au_{1-x}Cu_x$ samples, including standard values for the Au and Cu end members.

Analysis of the XRD data using Vegard's law (an empirical guideline that assumes a linear relationship between lattice constant and composition in alloys) provides one method for experimentally determining the compositions of the $Au_{1-x}Cu_x$ nanoparticles. Figure 2.4c shows a Vegard's law plot, which includes the lattice constants for the Au and Cu end members as well as for the $Au_{1-x}Cu_x$ samples. The XRD composition, included in table 2.1, can be estimated using Vegard's law as indicated on the plot in figure 2.4c.

2.3.3 Energy Dispersive X-Ray Spectroscopy

EDS analysis provides another method for experimentally analyzing the $Au_{1-x}Cu_x$ nanoparticle compositions. The EDS data, shown in figure 2.5a and included in table 2.1, indicates an increasing amount of Cu in each sample and is qualitatively consistent with the Vegard's law data. Figure 2.5b shows the copper content of the $Au_{1-x}Cu_x$ samples determined by EDS analysis plotted against the refined lattice constant determined from

the XRD data. This plot includes error bars that indicate the variance in the measured quantities, which will be discussed in more detail later.

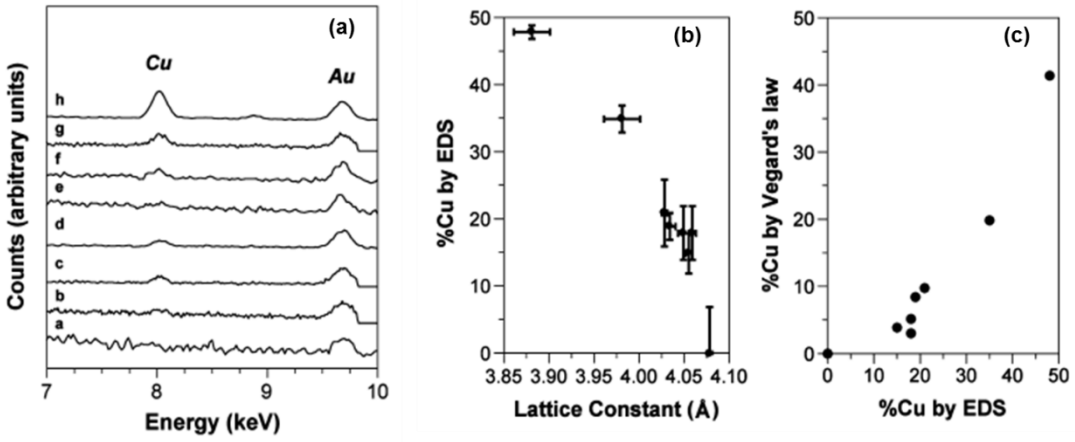

Figure 2.5 EDS data (a) for all $Au_{1-x}Cu_x$ samples. Plots of (b) EDS composition vs. lattice constant from the XRD data and (c) XRD-derived composition (Vegard's law) vs. EDS-derived composition. Panel (b) shows the raw data, along with error bars for each measurement. Panel (c) compares the compositions of each sample as determined independently by XRD and EDS analysis.

Interestingly, a plot comparing the Cu content determined by XRD vs. EDS analysis (figure 2.5c), as well as inspection of the data in table 2.1, shows that the two methods of composition analysis provide quantitatively different data. Qualitatively they show the same trend, but EDS indicates a higher Cu content than is estimated using Vegard's law, particularly at small values of x in $Au_{1-x}Cu_x$.

2.3.4 Analysis of Plasmonic Properties

For the pure Au nanoparticles, the comparison between theory and experiment is straightforward since the dielectric constant is available from the literature. The experimentally determined UV-Visible absorption data for the Au nanoparticles is shown in figure 2.6, together with the theoretical results obtained using Mie theory. In the

figure, the simulated absorption spectrum calculated with and without size-corrections is shown. Both theory and experiment find that the plasmon resonance is around 523 nm. It is also clear that the simulated spectrum that includes size-corrections is in much better agreement with the experimental result.

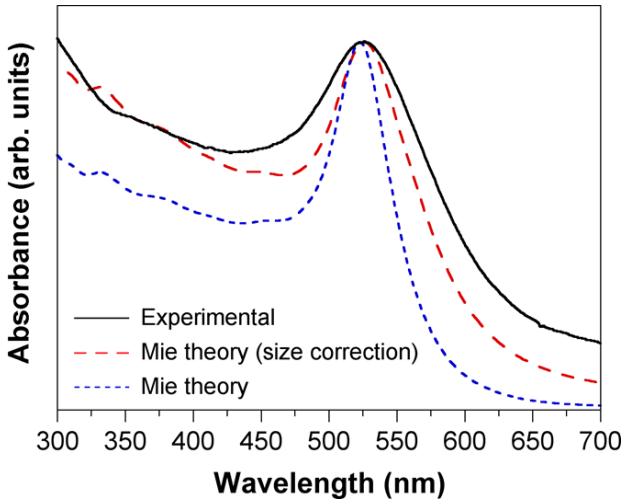

Figure 2.6 Experimental and simulated absorption spectra for Au nanoparticles (sample "a"). The experimental data are shown in black, the simulated spectrum using Mie theory is shown in blue, and the simulated spectrum using Mie theory with a size-corrected dielectric constant is shown in red.

Thus, as expected, size-corrections are important for the nanoparticles considered in this work. However, the experimental absorption spectrum is still slightly broader than the simulated spectrum. This is most likely due to the small dispersion in nanoparticle sizes, as indicated in figure 2.3, but the possibility of additional broadening caused by contributions not accounted for in the theoretical simulations can not be ruled out. The good agreement between theory and experiment, both with respect to peak position and the overall band shape, illustrates the generally high size uniformity and near spherical shape of the nanoparticles.

The experimentally determined UV-Visible absorption spectra for all of the $Au_{1-x}Cu_x$ samples are shown in figure 2.7a. This is compared with the simulated spectra for the $Au_{1-x}Cu_x$ samples where the compositions used in the simulations are those that have been determined using EDS (figure 2.7b) and XRD (figure 2.7c). In both cases, the dielectric constant used in the simulations was obtained using a simple linear mixing of the pure metal dielectric constants, which is considered to be the standard method for alloy nanoparticles.[25] The experimental absorption data in figure 2.7a visually suggest that λ_{max} red shifts as x increases, i.e. with increasing Cu content. This trend is expected, because the plasmon resonance frequency for Au is at 523 nm while for Cu it is found to be at 561 nm using Mie theory. However, quantitatively analyzing the peak maximum, e.g. the plasmon resonance frequency, is not straightforward because of the significant peak broadening and asymmetry for the samples with higher Cu contents.

For example, for sample "h", one could visually define the peak maximum as 545 nm, which is the actual λ_{max}, or closer to 560 nm, where the peak begins to visually decrease in intensity. The former is intermediate between Au and Cu, and the latter is close to that expected for pure Cu, which is not reasonable for this sample based on the experimental composition data that show an Au-Cu alloy with less than 50% Cu. Thus, to reliably determine the plasmon resonance frequency in a manner that is consistent across all samples, we fitted the experimental spectra to a high-order polynomial and defined the plasmon resonance frequency as the zero point of the derivative. When the peak maximum is analyzed using this quantitative algorithm, the apparent red shift of the plasmon resonance frequency is less significant for most of the samples (see table 2.1). When the errors associated with the composition measurements are taken into account,

there is very little shift of the peak maximum as the copper content increases up to 20-30%. At higher copper contents, e.g. 40 – 50%, the shift of the peak maximum is more significant.

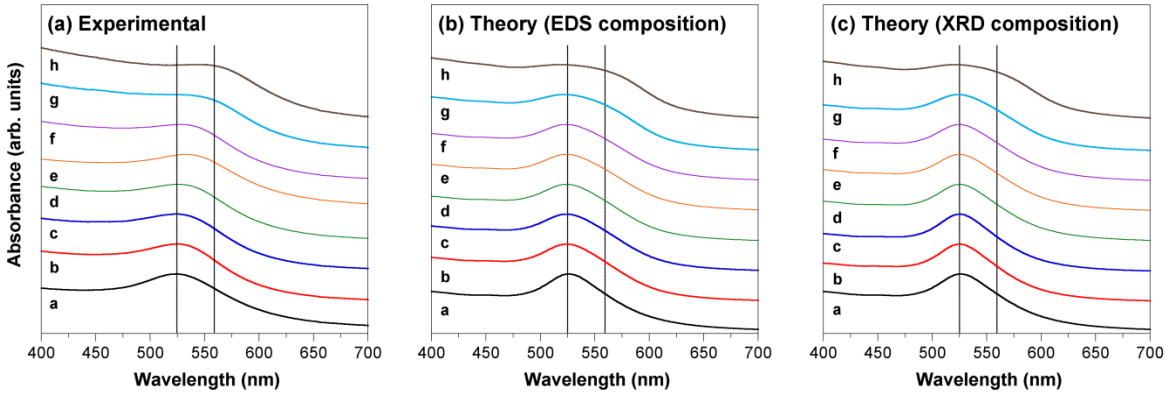

Figure 2.7 Experimental and simulated absorption spectra for $Au_{1-x}Cu_x$ nanoparticles: (a) experimental spectra, (b) simulated spectra using composition determined from EDS, and (c) simulated spectra using composition determined from XRD (Vergard's law). The vertical lines correspond to the plasmon frequencies of Au (523 nm) and Cu (561 nm).

Comparing both sets of simulated spectra – the set using the experimental XRD compositions (figure 2.7b) and the set using the experimental EDS compositions (figure 2.7c) – with the experimental results (figure 2.7a), we see that there is fair agreement between theory and experiment with respect to the overall shape of the absorption spectra. As the Cu content increases, the peak width increases. This phenomenon is attributable to two factors. First, Cu has larger interband contributions than Au. Second, as the Cu content increases the size of the nanoparticles decreases, and this results in additional damping due to increased surface scattering. For the simulated spectra, the peak position analysis (the zero point of the derivative of the high-order polynomial fit, identical to that described for analysis of the experimental spectra) showed that the peak position for all of the Au-Cu samples remained largely unchanged relative to the peak

position found for Au, even more so than was observed for the experimental absorption data. (For the experimental absorption spectra, the samples with the largest Cu contents showed a red shift in λ_{max}, while the corresponding simulated spectra do not.) This discrepancy – the fact that the experimental peak maximum does not match that predicted from a linear extrapolation between the peak maxima for pure Au and pure Cu, and the fact that the simulated spectra do not account for the red shift observed at higher Cu contents – is most likely due to inaccuracies in using a linear mixing rule to determine the dielectric constant for the Au-Cu alloys. Since the Drude terms for Au and Cu are very similar, the error is most likely associated with assuming a linear mixing rule for the interband contributions in the Au-Cu system. The interband contribution depends strongly on the exact electronic structure of the alloy and thus is not likely to be captured by simple linear mixing rule. Problems using the linear mixing rule when interband contributions are important have been noted before.[17,25]

In the simulated spectra, the peak positions all remain similar to those of pure Au, which indicates that the interband contribution of Au is overestimated in the simulations. The real interband contributions of the Au-Cu alloys, therefore, are most likely more similar to Cu, which is not accounted for by the linear mixing rule.

In figure 2.8 the experimentally-determined λ_{max} values as a function of the Cu composition determined independently using both XRD (blue squares) and EDS (red circles) is shown. Also plotted in the figure is a linear interpolation between the value for particles of pure Au (523 nm) and pure Cu (561 nm). Comparison of the data in figure 2.8 indicates that the XRD set and the EDS set are qualitatively similar, e.g. the general trends between composition and peak position are similar.

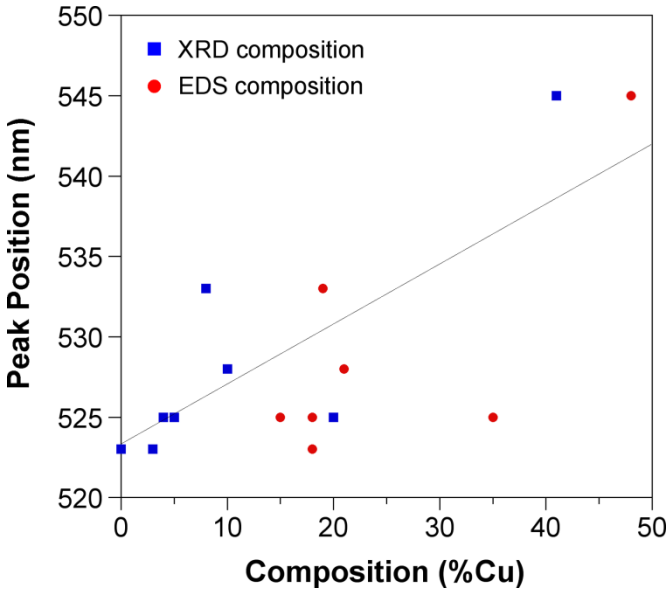

Figure 2.8 Experimentally determined plasmon resonance frequencies as a function of composition as determined independently by XRD (Vegard's law, blue squares) and EDS (red circles). The line corresponds to a linear interpolation between the plasmon frequencies of Au (523 nm) and Cu (561 nm).

However, the quantitative differences are important. Figure 2.8 shows that overall there is a better agreement between the experimentally determined λ_{max} values and what one would expect based on the XRD composition data, particularly for small values of x in $Au_{1-x}Cu_x$. This is consistent with the earlier observation that XRD tends to indicate less Cu than EDS, and is especially true when very little Cu is present. At higher Cu content, the EDS composition data seem to agree somewhat better with the expected trend. However, the large uncertainty in determining the absorption peak position due to the very broad resonance complicates the analysis. A comparison between the simulated and experimental absorption spectra presented in figure 2.8 also reflects this.

The data in figure 2.8 emphasize several important points. First, as highlighted in figure 2.5c and table 2.1, composition data as determined independently by EDS and XRD *via* Vegard's law are qualitatively similar, but quantitatively different. Second, for

$Au_{1-x}Cu_x$ samples with low Cu content, the XRD composition data more accurately correlate theory and experiment. This is reasonable, because for these samples, the values of x in $Au_{1-x}Cu_x$ are near the detection limit of EDS, where errors will be larger. This is validated by the error bars in figure 2.5b, which show greater uncertainty for the Au-rich samples (e.g. samples with small Cu content). Third, for the $Au_{1-x}Cu_x$ samples with higher Cu content, the EDS data are likely to be more reliable because the XRD peaks broaden significantly as more Cu is incorporated into the nanoparticles, and the error associated with accurately determining the lattice constants for these samples increases. This is validated by the error bars in figure 2.5b, which show greater uncertainty for the Cu-rich samples (e.g. samples with smaller lattice constants).

2.4 Synthesis and Examination of In_2Au Nanoparticles

2.4.1 Introduction

In addition to red-shifting the plasmon peak position of a noble metal, it should also be possible to blue-shift the plasmon peak position by incorporating a second metal that possesses a plasmon at a smaller wavelength than that of the first metal. This allows for the possibility of tuning the plasmonic properties of noble metal nanoparticles from the visible to the ultraviolet, expanding the potential applications of these materials.

Expanding on the previous efforts involving Au-Cu alloy nanoparticles, aqueous-phase gold nanoparticles were synthesized using a seed-mediated growth approach and by subsequently diffusing indium into the gold nanoparticles, it was possible to generate In_2Au nanoparticles. Although we were not able to achieve control over the shape or

optical properties of the resulting particles, we were able to demonstrate a blue-shift upon the incorporation of indium into the nanoparticles.

2.4.2 Synthesis of Aqueous Gold Nanoparticles

The gold nanoparticles were produced using a previously published seed-mediated approach.[41] Specifically a seed solution was first prepared using 2.5 mL of a 0.001 M solution of $HAuCl_4 \cdot 3H_2O$, 2.5 mL of 18 MΩ nanopure water and 5.0 mL of 0.20 M cetyltrimethylammonium bromide (CTAB). The resulting solution was allowed to stir vigorously while heated at 30°C in a warm water bath. For this method, it is critical that the solutions were kept at 30°C in order to prevent the CTAB from precipitating out of the solution. To initiate the nucleation of the Au seed particles, 60 μL of 0.10 M $NaBH_4$ (aq) was quickly injected into the solution. In order to ensure the proper growth rate of the resulting seeds, it was important that the $NaBH_4$ solution is cooled via ice bath before injection. The resulting seed solution was then aged for 2 min under stirring and an additional 5 min without stirring. After this time, 12 μL of the resulting seed solution was added to a growth solution.

The growth solutions were prepared by the combination of 5.0 mL of 0.001 M $HAuCl_4 \cdot 3H_2O$, 5.0 mL of 0.20 M CTAB, and 70 μL of 0.10 M ascorbic acid. The resulting solution was gently shaken and the color changed from yellow to colorless as the ascorbic acid solution was mixed. This indicated a reduction of Au^{3+} to Au^{1+}.[42] If the solution does not become completely colorless additional ascorbic acid should be added in increments of 5 μL. Once the solutions were colorless the seed solution was added to the growth solution and the resulting mixture was held at 30°C for one hour to ensure

complete nanoparticle growth. To increase the aspect ratio of the resulting rod-shaped nanoparticles, 0.004 μL of $AgNO_3$ can be added to the growth solutions in increments of 50 μL. It is important to note that this synthesis is sensitive to small amounts of impurities in the starting material. Consequently, the amounts used for this synthesis may need to be modified for the specific reagents used.

2.4.3 Synthesis of In_2Au Nanoparticles

The In_2Au nanoparticles were synthesized via a modified polyol approach. Specifically 25.0 mL of ethylene glycol and 20.0 mL of 35 wt% in H_2O poly(diallyldimethylammonium chloride) (PDDA) (M_W < 100,000) was placed in a 3-neck round bottom flask equipped with a reflux condenser. To this 59.0 mg of anhydrous indium chloride and 500 μL of the previously synthesized Au nanorod solution was added. The resulting solution was then heated under bubbling argon to 120°C over the course of 1 h. It is necessary that the solution be thoroughly purged with argon at this stage or In_20_3 impurities will result. 10 mL of a 2.5 mg/mL solution of $NaBH_4$ in tetraethylene glycol was then added to the solution dropwise over course of 10 min. The solution was then heated at 120°C for an addition 20 min before being cooled to room temperature. The resulting particles were precipitated via centrifugation at 10000 rpm for 15 min and were then dispersed in ethanol.

2.4.4 Results and Discussion

Representative TEM images of the resulting In_2Au nanoparticles and the aqueous gold nanorod precursors are shown in figure 2.9. These images illustrate that the Au nanorods become polysidperse in their morphology upon the incorporation of indium.

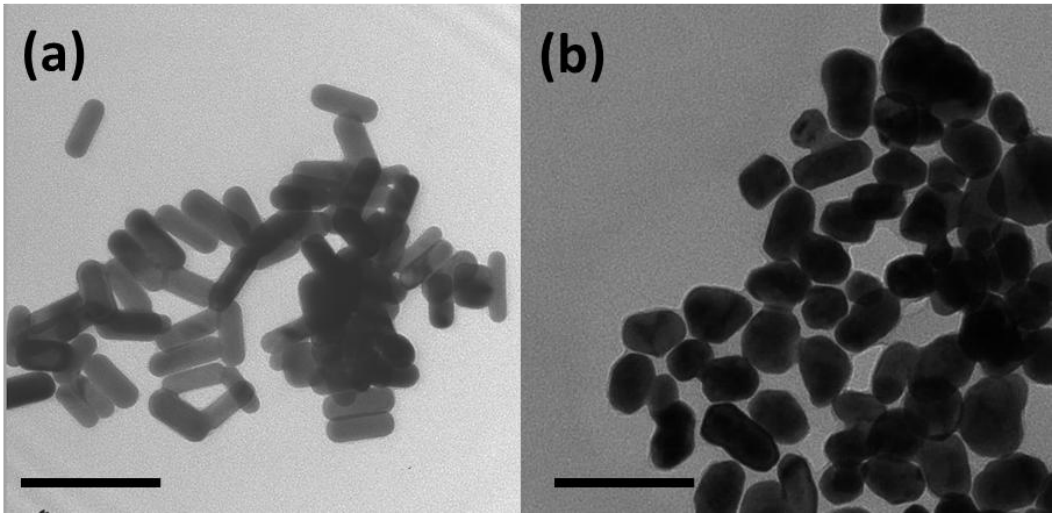

Figure 2.9 TEM images of (a) aqueous gold nanorods and (b) In_2Au nanoparticles demonstrating the loss of shape upon indium incorporation. Scale bars are 100 nm.

This resulting polydispersity and irregular morphology makes the In_2Au nanoparticles unsuitable for any detailed investigation of the optical properties of the material.

The powder X-ray diffraction pattern (figure 2.10) of the nanoparticles after the incorporation of indium confirms the presence of In_2Au. Although no other phases are observed in this XRD pattern, composition tunability in this system has so far been unachievable. This is consistent with the In-Au phase diagram, which contains several stoichiometric line phases rather than a continuously variable solid solution. When the amount of indium chloride is changed, either gold or indium impurities are observed in addition to the In_2Au. This inability to vary the composition of the resulting material

makes the In_2Au nanoparticles produced from this method unusable for the in-depth composition tunability examination that was performed on the composition tunable $Au_{(1-x)}Cu_x$ nanoparticles examined previously.

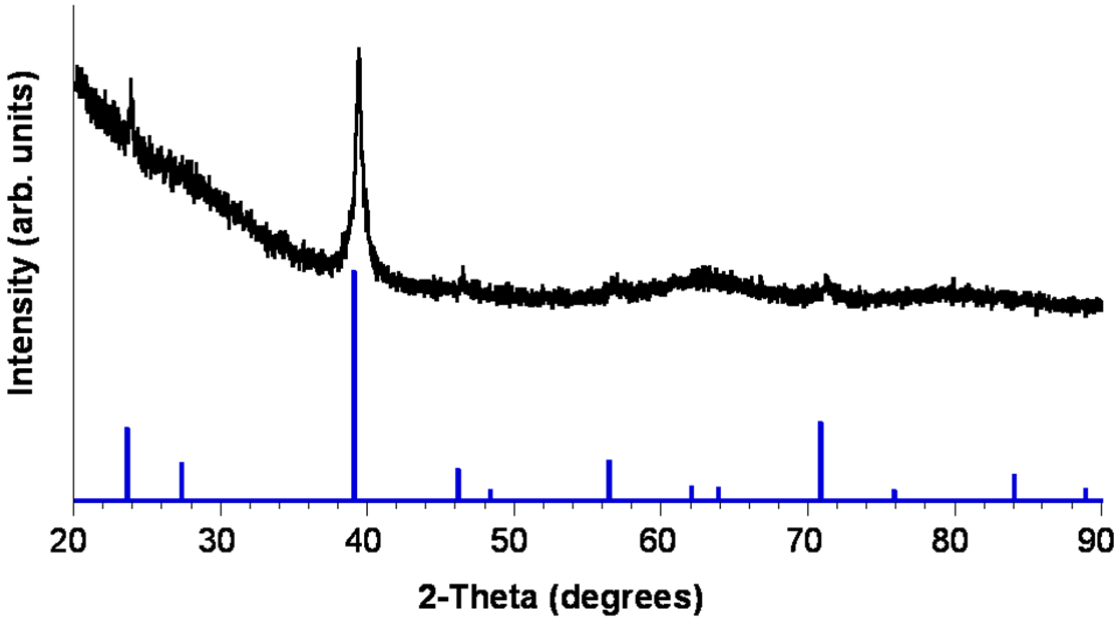

Figure 2.10 Powder X-ray diffraction pattern of In_2Au nanoparticles is shown in black. Simulated pattern for In_2Au is shown in blue.

The UV-Vis absorbance spectrum for the In_2Au nanoparticles (figure 2.11) does indicate that the plasmon absorbance peak can be blue-shifted into the UV by the incorporation of indium into the gold nanoparticles. The resulting peak has a λ_{max} of approximately 360 nm. The large amount of broadening that is present is likely due to the polydispersity and irregular shape of the resulting materials as well as a small degree of aggregation that is present.

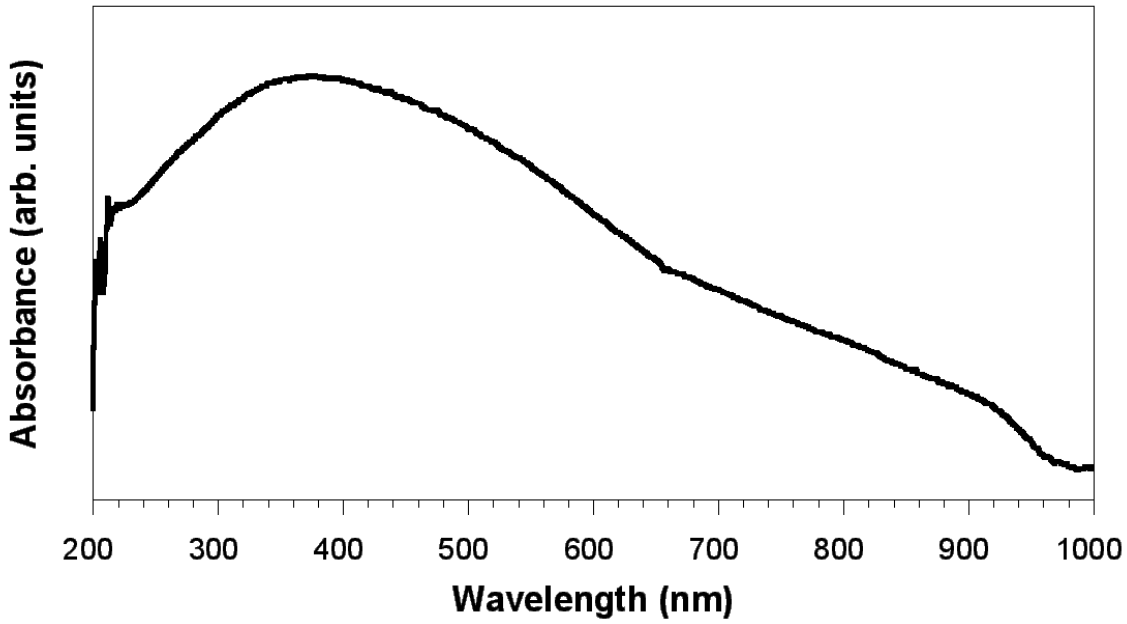

Figure 2.11 UV-Vis absorbance spectrum of In_2Au nanoparticles in ethanol, indicating plasmon peak in the UV.

The synthesis of In_2Au has served as a proof of concept, demonstrating the ability to blue-shift the plasmon absorbance peak of gold nanoparticles into the UV regime via changes in particle composition. Although control over the composition of this system may be difficult, it may be possible to enhance the shape retention of the gold nanorods by phase transferring the gold nanoparticles to a non-aqueous solvent before indium incorporation is attempted. This would allow for the use of alternate reducing agents and surfactants that have shown to be useful for shape control in similar systems.[43]

2.5 Conclusions

In this study the synthesis of a series of monodisperse spherical $Au_{1-x}Cu_x$ alloy nanoparticles was described. The uniform morphology allowed for a detailed examination of the relationship between compositional variation and the position of the

plasmon resonance frequency. The rigorous characterization in this study is necessary in order to bridge the gap between the experimentally obtained plasmon resonance frequencies of alloy nanoparticles and those predicted by theory. In providing such experimental comparison with theoretical calculations, several interesting conclusions about compositional measurements can be reached. First, application of Vegard's law to the refined lattice constants can be a reliable measure of composition for the lower copper content $Au_{1-x}Cu_x$ alloy nanoparticles. This technique becomes less reliable at higher copper contents due to the increased uncertainty in the lattice constant refinements that are the result of increased XRD peak broadening. The EDS measurements counteract this phenomenon by becoming slightly more accurate at the higher copper contents. Thus, a complete understanding of the composition variation in a given system will benefit from both EDS and XRD characterization techniques.

In addition, for the Au-Cu system, where the interband contribution of Cu significantly impacts the shape and breadth of the absorption peak, it is clear that a simple linear mixing of dielectric constants is not sufficient for theoretical modeling to accurately predict all of the details of the absorption spectra. This work can serve as a methodology template for future examinations of plasmonic alloy nanoparticle systems. Future systems can also be used to test existing theoretical models by examining more complex variations of composition and morphology. Such endeavors have the potential to improve our understanding of the creation and tunability of desirable optical properties in metal nanoparticle systems.

2.6 References

(1) Maier, S. A.; Brongerma, M. L.; Kik, P. G.; Meltzer, S.; Requicha, A. A. G.; Atwater, A. H. *Adv. Mater.* **2001**, *13*, 1501.

(2) Mekis, A.; Chen, J. C.; Kurland, I.; Fan, S.; Villeneuve, P. R.; Joannopoulos, J. D. *Phys. Rev. Lett*. **1996**, *77*, 3787.

(3) Alivov, Y.; Fan, Z. Y.; Appl. Phys. Lett. **2009**, *95*, 063504.

(4) Brown, P.; Takechi, K.; Kamat, P. V. *J. Phys. Chem. C* **2008,** *112*, 4776.

(5) Kneipp, K.; Wang, Y.; Kneipp, H.; Perelman, L. T.; Itzkan, I.; Dasari, R. R.; Feld, M. S. *Phys. Rev. Lett.* **1997**, *78*, 1667.

(6) Nie, S.; Emory, S. R. *Science*, **1997**, *275*, 1102.

(7) Lal, S.; Grady, N. K.; Kundu, J.; Levin, C. S.; Lassiter, J. B.; Halas, N. J. *Chem. Soc. Rev*. **2008**, *37*, 898.

(8) McFarland, A. D.; Young, M. A.; Dieringer, J. A.; Van Duyne, R. P. *J. Phys. Chem. B* **2005**, *109*, 11279.

(9) Zhang, X. Y.; Yonzon, C. R.; Van Duyne, R. P. *J. Mater. Res*. **2006**, *21*, 1083.

(10) (a) Le, F. ; Brandl, D. W.; Urzhumov, Y. A.; Wang, H.; Kundu, J.; Halas, N. J.; Aizpurua, J.; Nordlander, P. *ACS Nano* **2008**, *2*, 707. (b) Ni, W.; Kou, X.; Yang, Z.; Wang, J. *ACS Nano* **2008**, *2*, 677.

(11) Odom, T. W.; Nehl, C. L. *ACS Nano*, **2008**, *2*, 612.

(12) Prashant, K. J.; Huang, X.; El-Sayed, I. H.; El-Sayed, M. A. *Acc. Chem. Res*. **2008**, *41*, 1578.

(13) (a) Liang, H.; Wan, L.; Bai, C.; Jiang, L. J. *Phys. Chem. B* **2005**, *109*, 7795. (b) Csaki, A.; Garwe, F.; Steinbrück, A.; Maubach, G.; Festag, G.; Weise, A.; Riemann, I.; König, K.; Fritzsche, W. *Nano. Lett*. **2007**, *7*, 247. (c) Kang, B.; Mackey, M. A.; El-Sayed, M. A. *J. Am. Chem. Soc*. **2010**, *132*, 1517.

(14) Loo, C.; Lowery, A.; Halas, N.; West, J.; Drezek, R. *Nano Lett*. **2005,** *5*, 709.

(15) Hasan, W.; Stender, C. L.; Lee, M. H.; Nehl, C. L.; Lee, J.; Odom, T. W. *Nano Lett.* **2009**, *9*, 1555.

(16) (a) Juluri, B. K.; Zheng, Y. B.; Ahmed, D.; Jensen, L.; Huang, T. J. *J. Phys. Chem. C* **2008**, *112*, 7309. (b) Link, S.; Mohamed, M. B.; El-Sayed, M. A. *J. Phys. Chem. B* **1999**, *103*, 3073.

(17) Belotlov, V. I.; Carotenuto, G.; Nicolais, L.; Longo, A.; Pepe, G. P.; Perlo, P.; Zvezdin, A. K. *J. Appl. Phys.* **2006**, *99*, 044304.

(18) Link, S.; Wang, Z. L.; El-Sayed, M. A. *J. Phys. Chem. B* **1999**, *103*, 3529.

(19) (a) Xia, Y.; Xiong, Y.; Lim, B.; Skrabalak, S. E. *Angew. Chem. Int. Ed*. **2008**, *48*, 60. (b) Chen, Z.; O'Brien, S. *ACS Nano* **2008**, *2*, 1219. (c) Jana, N. R.; Gearheart, L.; Murphy, C. J. *J. Phys Chem. B* **2001,** *105*, 4065. (d) Tiwari, N.; Kalele, S.; Kulkarn, S. K. *Plasmonics* **2007**, *2*, 231.

(20) (a) Lim, B.; Camargo, P. H. C.; Xia, Y. *Langmuir*, **2008**, *24*, 10437. (b) Li, C.; Shuford, K. L.; Chen, M.; Lee, E. J.; Cho, S. O. *ACS Nano*, **2008,** *2*, 1760. (c) Sanjanlal, P. R.; Sreeprasad, T. S.; Nair, A. S.; Pradeep, T. *Langmuir*, **2008**, *24*,

4607. (d) Chu, H. C.; Kuo, C. H.; Huang, M. H. *Inorg. Chem*. **2006**, *45*, 808. (e) Millstone, J. E.; Wei, W.; Jones, M. R.; Yoo, H. Mirkin, C. A. *Nano Lett*. **2008**, *8*, 2526. (f) Smith, D. K.; Korgel, B. A. *Langmuir* **2008**, *24*, 644. (g) Bardhan, R.; Neuman, O.; Mirin, N.; Wang, H.; Halas, N. J. *ACS Nano* **2009**, *3*, 266. (h) Bakr, O. M.; Wunsch, B. H.; Stellacci, F. *Chem. Mater*. **2006**, *18*, 3297.

(21) Wiley, B.; Sun, Y.; Mayers, B.; Xia, Y. *Chem- Eur. J*. **2005**, *11*, 454.

(22) Yoo, H.; Millstone, J. E.; Li, S.; Jang, J. W.; Wei, W.; Wu, J.; Schatz, G. C.; Mirkin, C. A . *Nano Lett.* **2009**, *9*, 3038.

(23) Wang, X.; Zhang, Z.; Hartland, G, V.; *J. Phys. Chem. B* **2005**, *109*, 20324.

(24) (a) Wang, C.; Peng, S.; Chan, R.; Sun, S. *Small* **2009**, *5*, 567. (b) Mallin, M. P.; Murphy, C. J.; *Nano Lett.* **2002**, *2*, 1235. (c) Radziuk, D. V.; Zhang, W.; Schukin, D.; Möhwald, H. *Small* **2010**, *6*, 545. (d) Bok, H. M.; Shuford, K. L.; Kim, S.; Kim, S. K.; Park, S. *Langmuir* **2009**, *25*, 5266.

(25) Lee, K. S.; El-Sayed, M. A. *J. Phys. Chem. B* **2006**, *110*, 19220.

(26) Kim, M. J. ; Na, H. J.; Lee, K. C.; Yoo, E. A.; Lee, M. *J. Mater. Chem*. **2003**, *13*, 1789.

(27) Pal, U.; Sanchez-Ramirez, J. F.; Liu, H. B.; Medina, A.; Ascencio, J. A. *Appl. Phys. A: Mater. Sci. Process.* **2004**, *79*, 79.

(28) Sra, A. K.; Schaak, R. E. *J. Am. Chem. Soc.* **2004**, *126*, 6667.

(29) Chen, W.; Yu, R.; Li, L.; Wang, A.; Peng, Q.; Li, Y. *Angew. Chem. Int. Ed*. **2010**, *49*, 2979.

(30) Henkel, A.; Jakab, A.; Brunklaus, G.; Sönnichsen, C. *J. Phys Chem C* **2009**, *113*, 2200.

(31) Schaefer, Z. L.; Vaughn II, D. D.; Schaak, R. E. *J. Alloys Compd.* **2010**, *490*, 98.

(32) (a) Yang, W. H.; Schatz, G. C.; Van Duyne, R. P. *J. Chem. Phys. C* **1995**, *103*, 869. (b) Averit, R. D.; Westcott, S. L.; Halas, N. J. *J. Opt. Soc. Am. B* **1999**, *16*, 1824. (c) Coronado, E. A.; Schaz, G. C. *J. Chem. Phys*. **2003**, *119*, 3926.

(33) Bohen, C. F.; Huffman, D. R.; *Absorption and Scattering of Light by Small Particles*; John Wiley & Sons: New York, 1983.

(34) (a) Mulvaney, P. Lamgmuir, **1996**, *12*, 788. (b) Belotelov, V. I.; Carotenuto, G.; Nicolais, L.; Pepe, G. P.; Zvezdin, A.K. Eur. Phys. J. B, **2005**, *45*, 317.

(35) Gschneidner, K.A; Vineyard, G. H. *J. Appl. Phys.* **1962**, *33*, 3444.

(36) Okamoto, H.; Chakrabarti, D. J.; Laughlin, D. E.; Massalski, T. B.; *Phase Diagram of Binary Gold Alloys*; Okamoto, H.; Massalski, T. B.; Ed.; ASM International: Metals Park, OH, 1987; pp 76.

(37) Sra, A. K.; Ewers, T. D.; Schaak, R. E.; *Chem. Mater*. **2005,** *17*, 758.

(38) Johnson, P. B. ; Christy, R. W. Phys. Rev. B, **1972**, *6*, 4370.

(39) Kreibig, U.; Fragstein, C. V. Z. Physik, **1969**, *224*, 307.

(40) Liu, Q.; Yan, Z.; Henderson, N. L.; Bauer, J. C.; Goodman, D. W.; Batteas, J. D.; Schaak, R. E. *J. Am. Chem. Soc*. **2009**, *131*, 5720.

(41) Nikoobakht, B.; El-Sayed, M. A. *Chem. Mater*. **2003**, *15*, 1957.

(42) Gole, A.; Murphy, C. J. *Chem. Mater*. **2004**, *16*, 3633.

(43) Motl, N. E.; Bondi, J. F.; Schaak, R. E. *Chem. Mater*. **2012**, *24*, 1552.

Chapter III

Synthesis of Colloidal Au-Cu_2S Heterodimers *via* Chemically Triggered Phase Segregation of AuCu Nanoparticles

3.1 Introduction

Colloidal hybrid nanoparticles are comprised of multiple domains fused together through a solid-state interface.[1-5] This direct contact facilitates electronic and magnetic communication between components that can result in enhanced and synergistic properties.[6] As a result, such hybrid nanoparticle systems are emerging as powerful multi-functional materials for applications that include biomedicine, catalysis, solar energy conversion, electronics, and magnetism.[1-8] Colloidal hybrid nanoparticles are typically synthesized by the controlled heterogeneous nucleation of one nanoparticle onto the surface of another.[1-4] Other strategies include the fusion of two pre-made particles[9] and the surface de-wetting of a core-shell nanoparticle.[10] All of these methods rely sensitively on the chemistry of the nanoparticle surfaces. Accordingly, issues such as lattice matching, heating profile, size and crystallinity of the nanoparticle seeds, and concentration, purity, and chemistry of the solvent, stabilizer, and reagents – all of which can be difficult to reproducibly control[11] – influence the morphology of the product, including nucleation density and product distribution.

---

[*] Reproduced in part with permission from Chem. Mater. 24, N.E. Motl, J.F. Bondi, R.E. Schaak, Synthesis of Colloidal Au-Cu_2S Heterodimers *via* Chemically Triggered Phase Segregation of AuCu Nanoparticles,1552-1554, Copyright 2012 American Chemical Society.

An alternative route to colloidal hybrid nanoparticles is to begin with an alloy nanoparticle, then induce phase segregation to form a two-component product. This strategy would allow one to pre-program the composition of the desired materials components in the alloy nanoparticle seed, then chemically trigger its segregation into two distinct particles that remain adjoined. Such an approach could capitalize on the growing number of available colloidal alloy and intermetallic nanoparticles as a diverse library of nanoparticle precursors[12] and the growing number of nanoparticle transformation reactions as a diverse toolbox of chemical triggers.[13] This approach would also shift the driving force for hybrid nanoparticle formation from heterogeneous nucleation to phase segregation, minimizing some of the surface chemistry issues involved with colloidal heterogeneous nucleation.

Several prior reports suggest that this process should be feasible, including the conversion of (a) AuCu particles to biphasic Au-Cu_2O *via* a gas phase high temperature melting/oxidation process,[14] (b) AuCd alloy nanoparticles to Au-CdSe core-shell particles *via* reaction with Se at 250 °C,[15] (c) Au nanoparticles to Au@$CuInSe_2$ core-shell particles *via* reactions of Au-Cu surface alloys,[16] and (d) CdS to CdS-CdTe heterodimers *via* partial S/Te ion exchange.[17] Additional examples of nanoscale phase segregation reactions suggest that such a process should be general, including the oxidation of CoAl to Co-Al_2O_3,[18] AuNi to Au-NiO,[19] AuSn to Au-SnO_2,[20] PtBi to Pt-Bi_2O_3,[21] and Bi_2Pd to Pd-Bi_2O_3.[21] However, while core-shell particles and composites are frequently observed products, to our knowledge, colloidal hybrid nanoparticles have not yet been synthesized using a solution-mediated chemically triggered phase segregation reaction. Here, we show that uniform colloidal AuCu alloy nanoparticles react with dissolved sulfur and

bubbling oxygen to form uniform colloidal hybrid Au-Cu_2S nanoparticles. Au-Cu_2S serves as an important prototype system, because it merges the known visible-wavelength plasmonic properties of Au nanoparticles[22,23] with the p-type semiconductor chalcocite, Cu_2S, which is of interest as a non-toxic and earth-abundant light absorber for applications in solar energy conversion.[24,25]

3.2 Experimental Details

3.2.1 Materials Used

Hydrogen tetrachloroaurate trihydrate [99.99%, $HAuCl_4 \cdot 3H_2O$], copper (II) acetate [98%, $Cu(OOCCH_3)_2 \cdot H_2O$], oleic acid [tech. 90%, $C_{18}H_{34}O_2$] and 1-octadecene [tech. 90%, $C_{18}H_{36}$] were purchased from Alfa-Aesar. Oleylamine [tech. 70%, $C_{18}H_{37}N$] and trioctylamine [98%, $C_{24}H_{51}N$] were purchased from Sigma-Aldrich. Methylthioninium chloride (methylene blue) [85%, $C_{16}H_{18}ClN_3S \cdot 3H_2O$] was purchased from Aldrich.

3.2.2 Synthesis of Au-Cu_2S Heterodimers

Figure 3.1 shows a schematic of the synthetic approach that chemically transforms AuCu nanoparticles into Au-Cu_2S heterodimers. First, AuCu nanoparticles are

synthesized using a modification of a published two step procedure.[26]

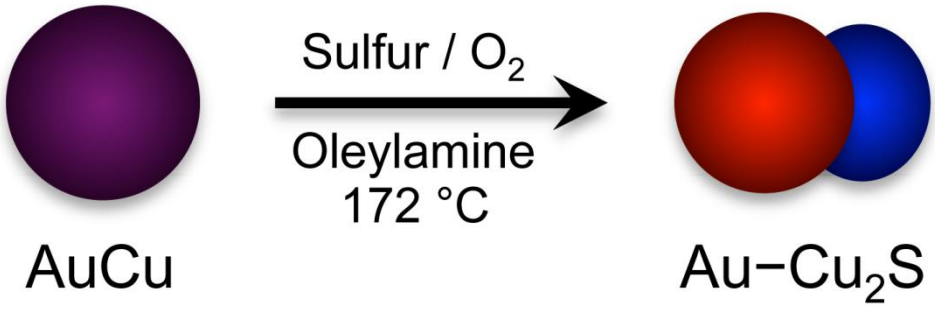

Figure 3.1 Schematic showing the synthesis of Au-Cu_2S heterodimers from AuCu nanoparticle precursors.

1.00 g of $HAuCl_4 \cdot 3H_2O$ was dissolved in 100 mL of 1-octadecene and 100 mL of oleylamine. The solution was then stirred vigorously and heated to 120 °C at a ramp rate of 6.7 °C/min. The solution was then held at this temperature for 45 min and subsequently allowed to cool to room temperature. The resulting Au particles were isolated with centrifugation and washed several times with ethanol. 90 mg of copper (II) acetate was then dissolved in 20 mL of trioctylamine and 4 mL of oleic acid and subsequently heated to 80 °C to ensure complete dissolution.

A dispersion containing 93 mg the previously synthesized Au particles in 8 mL of hexanes was added to the copper (II) acetate solution, which was then heated to 120 °C over 20 min to remove the hexanes and any residual water. The solution was then placed under argon and heated to 260 °C at a ramp rate of 1.7 °C/min. The solution was then cooled to room temperature. The resulting particles were isolated with centrifugation and washed several times with ethanol.

Next, a solution containing 5.8 mg of sulfur in 20 mL of oleylamine is added to a dispersion containing 17 mg of the AuCu nanoparticles in 5 mL of hexanes. After

heating to 120 °C over 90 min to remove the hexanes and any residual water, the solution is heated to 172 °C at a ramp rate of 1.5 °C/min and subsequently cooled to room temperature as soon as this temperature is reached. Air is continuously bubbled through the flask during the entire course of the reaction, perhaps serving to activate the reaction by forming an oxide surface or intermediate. The particles are isolated by centrifugation and washed several times with ethanol.

3.2.3 Characterization

Powder X-ray diffraction (XRD) patterns were obtained at room temperature using a Bruker-AXS D8 Advance diffractometer with Cu Kα radiation and a LynxEye 1-D detector. Refined lattice constants were obtained using Chekcell.

Transmission electron microscopy (TEM) images were obtained using a JEOL 1200 EX-II microscope operating at an accelerating voltage of 80 kV. Dark-field and bright-field HRTEM images and EDS spectra were performed on a JEOL EM-2010F STEM operating at 200 kV with a typical probe size of 0.7 nm and an EDAX solid-state X-ray detector. Spot scans and line scans were conducted and referenced with drift correction to account for any sample displacement. Data analysis was carried out using ESVision software (copyright Emispec, 2004).

UV-Vis absorption spectra were collected using an Ocean Optics HR4000 spectrometer with a Micropack DH-2000 BAL UV-Vis NIR light source. Nanoparticle samples were dispersed in hexanes for UV-Vis data collection unless otherwise indicated.

UV-Vis-NIR absorbance measurements were collected on a Perkin-Elmer Lambda 950 spectrophotometer equipped with a 150 mm integrating sphere. Nanoparticle samples were dispersed in toluene for data collection.

Samples for TEM and STEM were prepared by drop-casting hexane-dispersed nanoparticles onto nickel TEM grids. Lattice spacings were measured from the fast-fourier transform (FFT) of HRTEM images, using Gatan Digital Micrograph^{TM} software. Energy Electron Loss Spectroscopy (EELS) was carried out on Au-Cu dimers using a JEOL EM-2010F STEM operating at 200 kV with a probe size of 0.7 nm and a Gatan Model EnfinaTM 1000 system. Single spot analysis was performed on the Au and Cu regions of the as-made dimers. All EELS analyses were referenced to C at 284.2 eV (K 1s).

3.2.4 Acknowledgement of Author Contributions

Nathan Motl, James Bondi, Eric Popczun, and Su-Il In contributed to the work presented in this chapter. Nathan Motl synthesized all of nanoparticles and heterodimers and preformed the control reactions. EDS and EELS measurements were taken by James Bondi. TEM and XRD measurements were taken by Nathan Motl. Refined lattice constants were obtained using Chekcell as performed by Nathan Motl. HRTEM and STEM measurements were taken by James Bondi. UV-Vis-NIR absorption measurements we collected by Eric Popczun. Photodegredation experiments were performed by Nathan Motl with assistance from Su-Il In.

3.3 Results and Discussion

3.3.1 Electron Microscopy

Representative transmission electron microscopy (TEM) images of the Au-Cu_2S product are shown in figures 3.2a and 3.2c, along with a TEM image of the AuCu nanoparticle precursor in figure 3.2b.

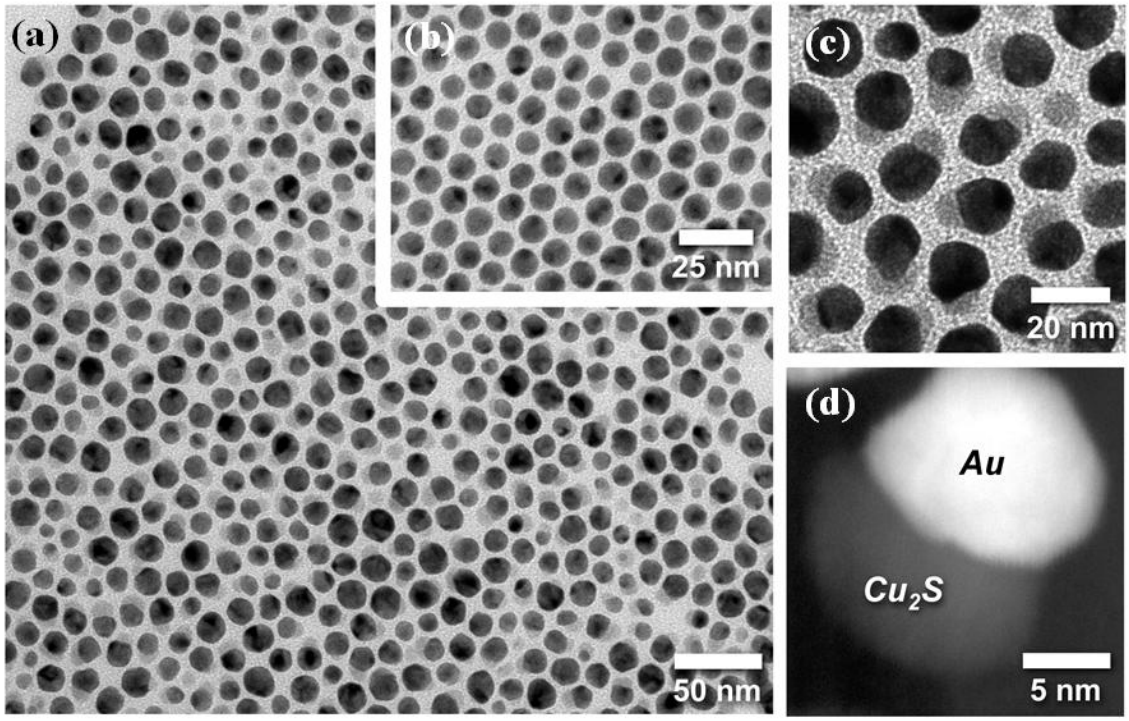

Figure 3.2 Representative TEM images of (a) the Au-Cu_2S heterodimers and (b) the AuCu nanoparticle precursors. A higher magnification TEM image of the Au-Cu_2S heterodimers is shown in (c) along with a representative dark-field TEM image in (d).

The AuCu nanoparticles are uniform and spherical with an average diameter of 10 ± 1 nm, while the product nanoparticles appear biphasic. The larger darker-contrast components (Au) have an average diameter of 10 ± 2 nm, and the smaller lighter-contrast components (Cu_2S) have an average width of 4 ± 1 nm and an average length of 7 ± 2 nm, respectively. Histograms of the components are shown below in figure 3.3.

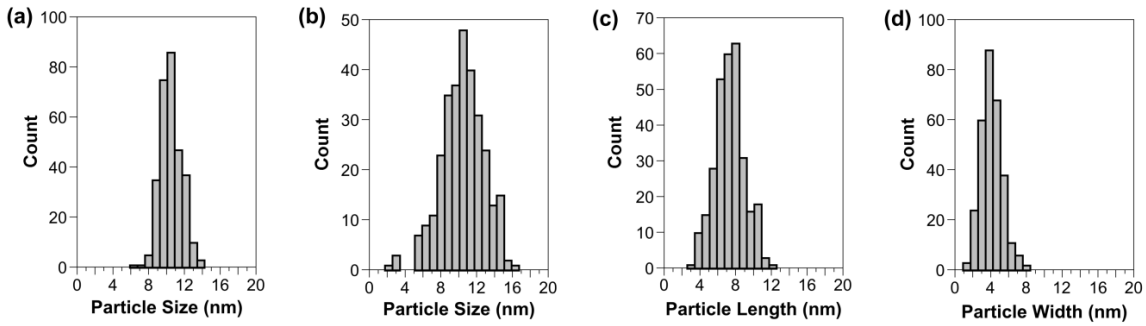

Figure 3.3 Particle size histograms: (a) AuCu nanoparticle precursors, (b) Au domain of Au-Cu_2S heterodimer products, and Cu_2S domain (c) length and (d) width.

The Au-Cu_2S heterodimers comprise 80% of the sample, with 17% and 3% of the sample corresponding to ~12 nm darker-contrast particles (either Au or AuCu) and ~7 nm Cu_2S particles, respectively. The small amount of free Cu_2S particles is likely to originate either from de-wetting from the Au component of the Au-Cu_2S dimers or from a separate nucleation event caused by the reaction of sulfur with a minimal amount of free dissolved copper species.

The representative dark field TEM image in figure 3.2d shows a bright region, consistent with the higher-Z (Z = atomic number) Au component, and a darker region, consistent with the lower-Z Cu_2S component. The high resolution TEM (HRTEM) images in figure 3.4 further confirm that the hybrid nanoparticles are comprised of Au and Cu_2S.

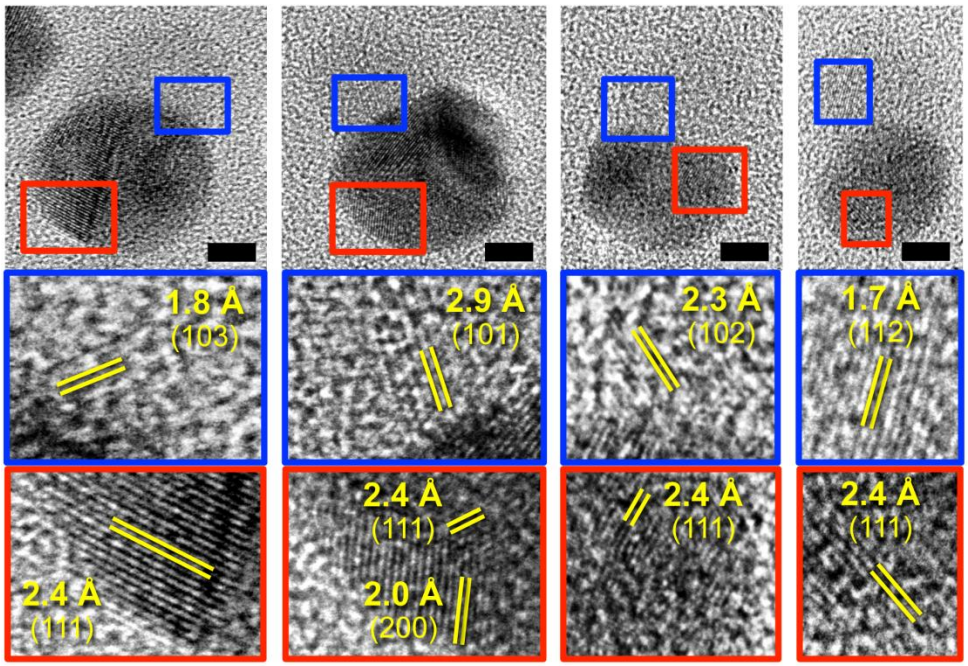

Figure 3.4 HRTEM images of several Au-Cu_2S heterodimers. The enlarged regions below each heterodimer highlight lattice fringes from the Au (red outline) and Cu_2S (blue outline) regions, as indicated. The scale bars correspond to 4 nm.

The darker-contrast regions exhibit lattice spacings of 2.0 Å and 2.4 Å, which are consistent with the (200) and (111) planes of Au, respectively (ICDD PDF Card #71-4615). The lighter-contrast regions exhibit lattice spacings of 1.7 Å, 1.9 Å, 2.4 Å, and 2.9 Å, which are consistent with the (112), (103), (102), and (101) planes of Ni_2In-type Cu_2S (β-Cu_2S), respectively (PDF #26-1116).

3.3.2 Powder X-Ray Diffraction

Powder XRD data for the AuCu precursor (figure 3.5) yields lattice constants of a = 3.925(7) Å and c = 3.710(5) Å, which is consistent with the tetragonal $L1_0$ intermetallic phase with approximately 1:1 stoichiometry (PDF #65-2798).

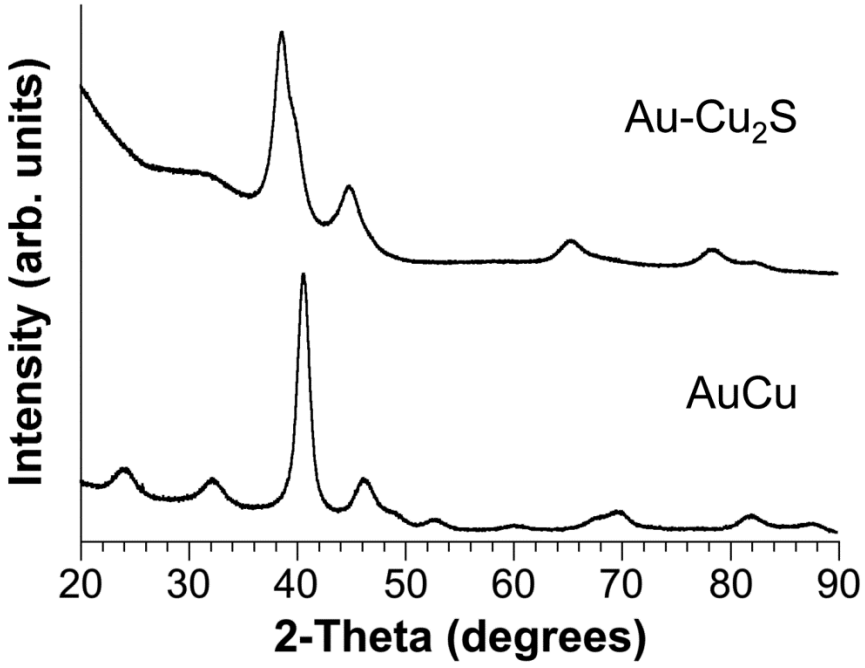

Figure 3.5 Powder XRD data for the Au-Cu_2S heterodimers and the AuCu nanoparticle precursors.

Powder XRD data for the Au-Cu_2S product shows no evidence of Cu_2S, which is reasonable given the small particle size and polycrystallinity of the Cu_2S domain as identified by HRTEM, coupled with the lower symmetry structure of β-Cu_2S relative to fcc-Au. The predominant phase is cubic with a = 4.053(3) Å, which is close to that of Au (a_{lit} = 4.073 Å, PDF #71-4615). A secondary phase with a = 3.94(6) Å is consistent with an $Au_{1-x}Cu_x$ alloy with $x \approx 0.28$ (estimated using Vegard's law), and likely corresponds to the free dark-contrast particles identified in the TEM image in figure 3.2a. The XRD data implies that the dark-contrast component of the hybrid particles is predominantly Au, although it is likely that a small amount of Cu remains alloyed with the Au.

3.3.3 Energy Dispersive X-Ray Spectroscopy

Further compositional characterization of the hybrid nanoparticle products is shown in figures 3.6 and 3.7. The energy dispersive X-ray spectrum (EDS) taken across a Au-Cu_2S heterodimer (figure 3.6) shows that the Au signal is localized to the darker-contrast region and the Cu signal is predominantly localized to the lighter-contrast region. The Cu signal does not disappear in the Au region, which could originate from an overlapping Ni signal or indicate that a small amount of Cu remains alloyed with the Au. However, control experiments typically show a small Cu signal on blank Ni TEM grids, which suggests that the low Cu signal in the Au region may be attributed to background or some of the Cu_2S component wrapping around the Au domain.

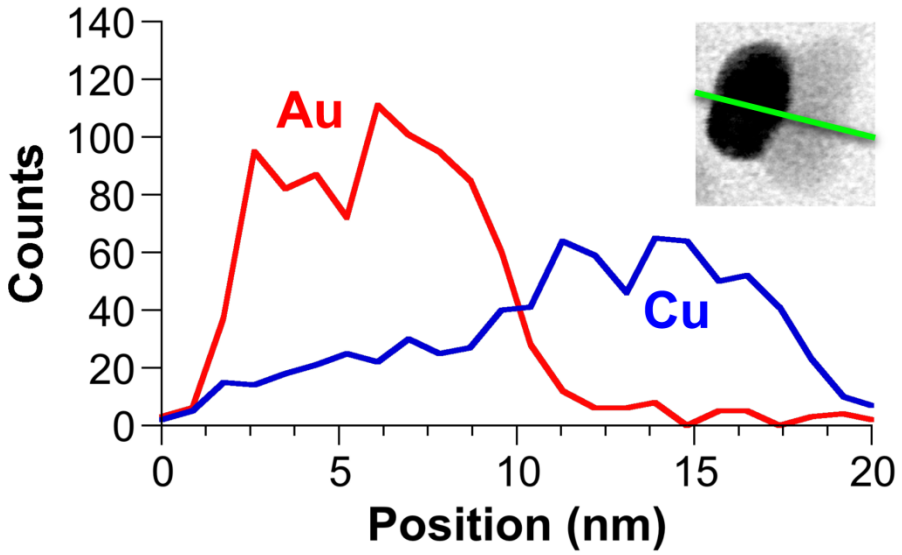

Figure 3.6 EDS line scan across a representative Au-Cu_2S dimer, as indicated on the accompanying TEM image.

The representative EDS data taken from the lighter-contrast region, labeled as spot "A" in figure 3.7, shows only signals for Cu and S, along with Ni from the TEM

grid. No Au is present in this region. EDS data from the darker-contrast region, labeled as spot "B" figure 3.7, shows only signals for Au and Ni, without evidence of Cu and S. The EDS data are consistent with a phase-segregated Au-Cu_2S heterodimer.

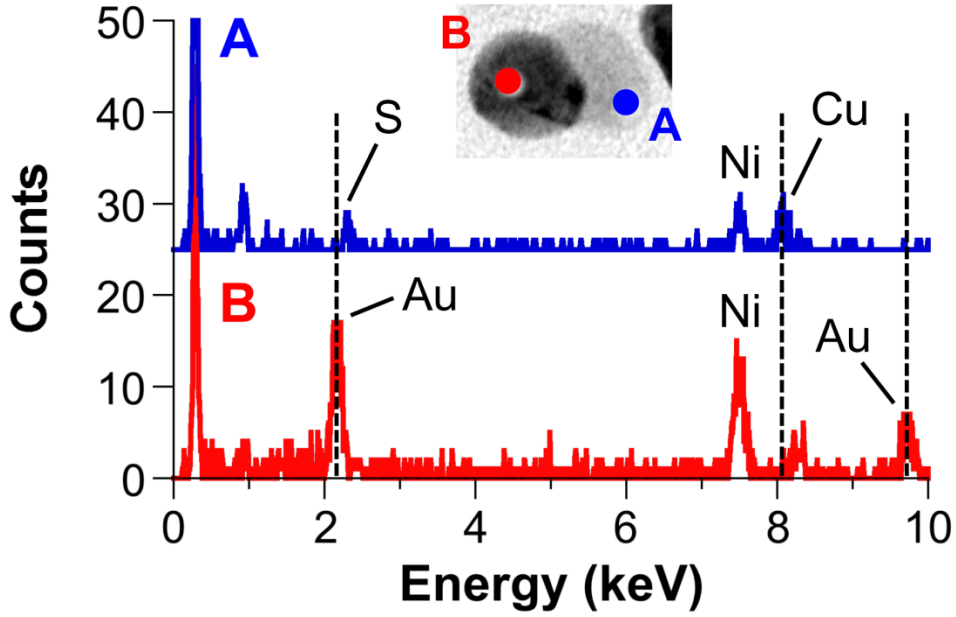

Figure 3.7 EDS spectra for the Cu_2S and Au regions indicated on the accompanying TEM image as spot "A" and spot "B", respectively. The Ni signal is background from the TEM grid, and the EDS spectra show Cu and S (without Au) in the Cu_2S domain and Au (without Cu and S) in the Au domain.

3.3.4 Electron Energy Loss Spectroscopy

Electron energy loss spectra (EELS) of the Au regions (figure 3.8a) also show a weak signal corresponding to Cu (932.7 eV, L_3 $2p_{3/2}$ and 952.3 eV, L_2 $2p_{1/2}$), but the Cu signal intensity increases significantly at both 932.7 and 952.3 eV when EELS spectra are acquired from the Cu_2S region (figure 3.8b). Importantly, the lower energy region of the EELS Cu scan acquired from the Cu_2S region shows a clear sulfur edge at 163.6 eV (L_1 $2p_{1/2}$) (figure 3.8c), but no evidence for oxygen at 543.1 eV (K 1s) (figure 3.8c). This is consistent with the presence of copper sulfide and not copper oxide.

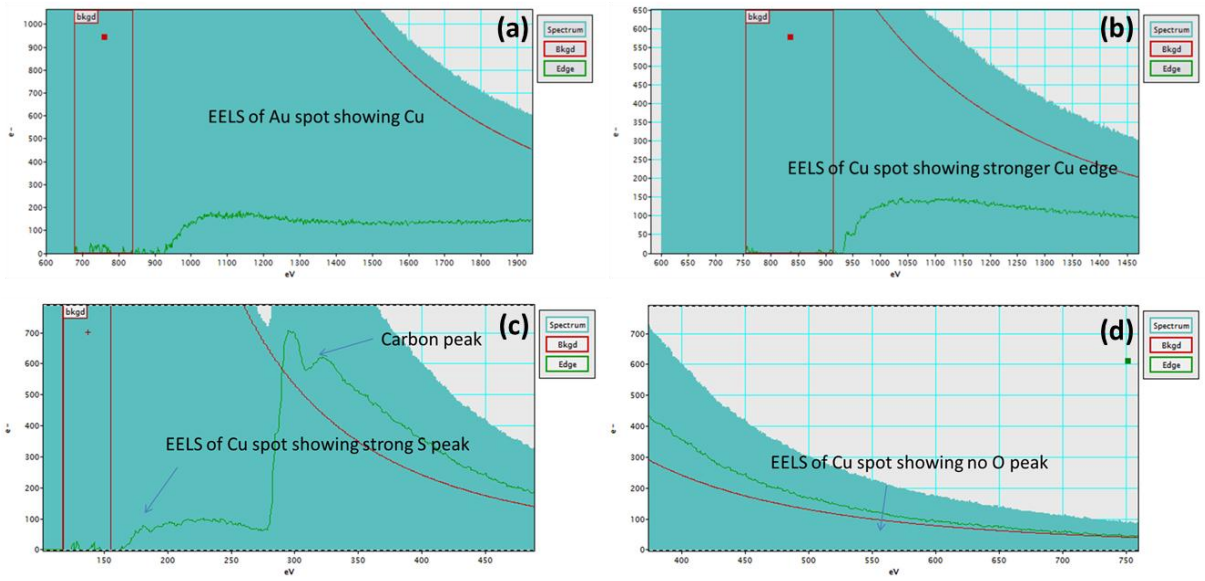

Figure 3.8 Electron energy loss spectra of Au region (a) and Cu_2S (b-c) region of Au-Cu_2S heterodimers.

3.3.5 UV-Vis Spectroscopy

UV-Vis absorbance spectra of the nanoparticles produced are shown in figure 3.9. The spectra indicate a maximum absorbance of ~520 nm for the Au nanoparticles and ~550 nm for the AuCu nanoparticles. The Absorbance spectrum for the Au-Cu_2S shows a slight blue-shift and more pronounced plasmon peak, indicating a loss of copper in the material.

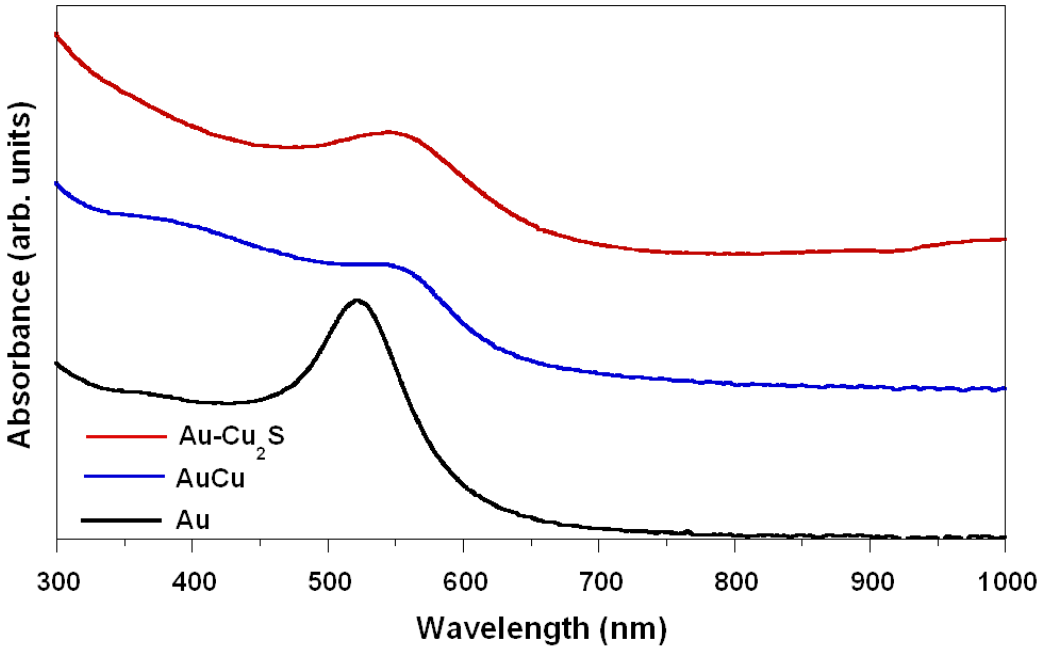

Figure 3.9 UV-Vis absorbance spectra of Au nanoparticles, AuCu nanoparticles and Au-Cu_2S heterodimers.

3.3.6 UV-Vis-NIR

A UV-Vis-NIR absorption spectrum (figure 3.10) provides additional support for the formation of β–Cu_2S *via* comparison with literature reports.[30, 31] However, the possibility exists that other Cu-S phases or a mixture, could be present.

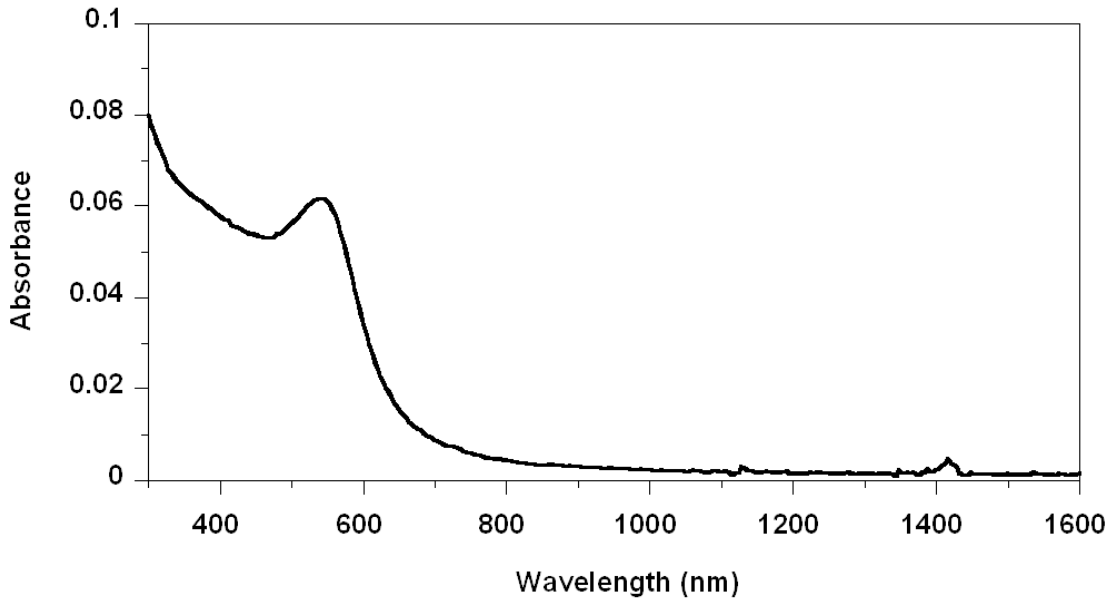

Figure 3.10 UV-Vis-NIR spectrum for Au-Cu_2S heterodimers. The lack of an observable absorption feature above 1000 nm suggests that Cu_2S is the predominant copper sulfide phase present.

3.3.7 Control Experiments

The data presented above is consistent with the transformation of AuCu nanoparticles into Au-Cu_2S heterodimers *via* a chemically induced phase segregation pathway. However, an alternate reaction pathway is one in which the Au-Cu_2S heterodimers form through a dissolution and re-precipitation process, e.g. the Cu is leached from the AuCu nanoparticles and Cu_2S is deposited upon reaction with sulfur. To test this possibility, Au nanoparticles were reacted with dissolved copper (II) acetate under otherwise identical conditions. A representative TEM image of the resulting particles is shown in figure 3.11a. Although this reaction produces a very small amount (16%) of Au-Cu_2S heterodimers, the predominant product (71%) is Au nanoparticles that do not contain adjoined Cu_2S, along with a small amount (13%) of Cu_2S particles. This product distribution is very different from that of the product formed by reacting AuCu

nanoparticles with sulfur (80% Au-Cu_2S heterodimers), suggesting that while heterogeneous nucleation may compete with phase segregation, phase segregation is likely the predominant reaction pathway.

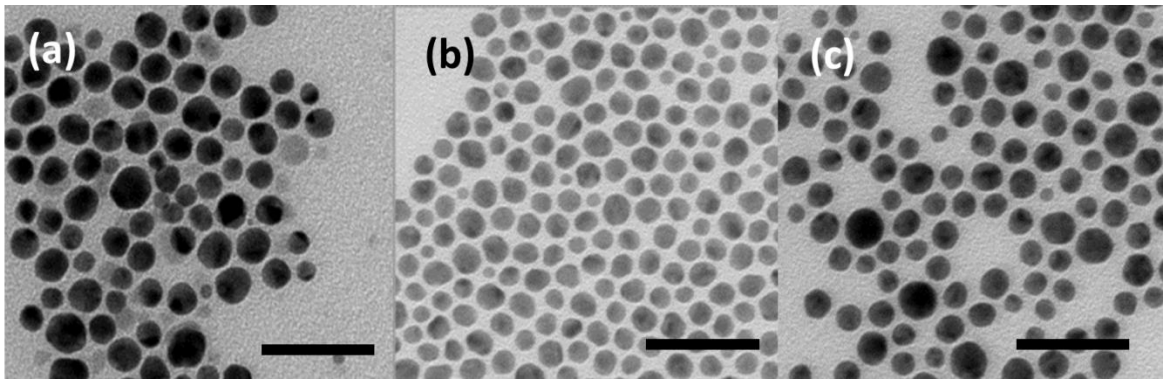

Figure 3.11 Representative TEM images of nanoparticles that result from control reactions with (a) copper (II) acetate, (b) argon bubbling, and (c) the absence of sulfur. Scale bars are 50 nm.

In order to further probe the mechanism of this phase segregation, specifically the necessity of air bubbling in the phase segregation, further experiments were performed. Specifically, the dimer synthesis was repeated with argon bubbling in the place of air bubbling, with all other reaction parameters held constant. A representative TEM image of the material is shown in figure 3.11b. The resulting particles show no indication of dimer formation. This result indicates that the presence of oxygen is necessary for the formation the heterodimers. It is plausible that the copper is oxidized to Cu_2O as an intermediate before subsequent conversion to Cu_2S occurs. If this is the case, it may be possible to isolate an Au-Cu_2O heterodimer if no sulfur is added. In order to examine this possibility, the synthesis was repeated without the addition of sulfur, with all other reaction parameters held constant. A representative TEM image of the material is shown in figure 3.11c. The resulting particles show no evidence of dimer formation, or any

indication of oxide formation. It is possible that only the surface copper atoms are oxidized, and no phase segregation occurs until it is converted to Cu_2S.

3.3.8 Sample Calculations

The relative sizes of the Au and Cu_2S components in the Au-Cu_2S heterodimers are also consistent with a phase segregation pathway. A simple calculation suggests that complete extraction of Cu from spherical 10 nm particles of stoichiometric AuCu would yield ~8 nm spherical Au particles. For an average AuCu particle, the radius is 5 nm, which yields a volume of 5.23×10^{-19} cm^3. The density of AuCu is 15.0 g/cm^3,[27] which corresponds to 3.01×10^{-20} mol Cu per average AuCu particle. If every two moles of Cu react with one mole of S to form Cu_2S, the volume of the Cu_2S domain that would form per AuCu particle is 4.13×10^{-19} cm^3, based on a Cu_2S density of 5.79 g/cm^3.[28] This corresponds to a spherical Cu_2S nanoparticle with a diameter of 9 nm. The number of moles of Au that would remain after full extraction of Cu (3.01×10^{-20} mol) would produce a spherical particle with a diameter of 8 nm, based on an Au density of 19.3 g/cm^3.[29]

XRD and EDS data (figures 3.5, 3.6, and 3.7) indicate that a small amount of Cu may remain in the Au domain, and the actual particles are not rigorously spherical. Therefore, only a small decrease in the average size of the Au-containing domain (within the statistical size distribution of the AuCu nanoparticle precursors) is expected upon phase segregation, and this is what is observed. Also, a similar calculation suggests that if all of the Cu within the AuCu nanoparticles reacts with sulfur to form Cu_2S, spherical 9-nm Cu_2S particles would form. The Cu_2S domain of the Au-Cu_2S heterodimers is not

spherical, but has an average size of $4 \pm 1 \times 7 \pm 2$ nm. This is on par with the amount of Cu in the AuCu nanoparticles that reacts with sulfur.

3.3.9 Photocatalysis of Methylene Blue

The catalytic properties of the produced Au-Cu_2S heterodimeres were also investigated. The enhancement of photocatalysts through hybrididzation with a Au domain is well known. A recent example[25] of this has shown that Au-Cu_2S core-shell structures can act as a photocatalyst in the degradation of methylthioninium chloride (methylene blue). As a test case, the Au-Cu_2S heterodimers were utilized as a photocatalyst for the degradation of methylene blue.

In a typical photodegradation experiment, a dispersion of 0.15 mg of Au-Cu_2S heterodimers in 38 μL of hexanes were added to 2 mL of a 1.6×10^{-3} mg/ml of methylene blue solution in ethanol and placed inside a quartz cuvette. The cuvette was sealed and illuminated with light at a wavelength of $\lambda > 400$ nm using a 300 W Xe lamp (intensity is 100 mW/cm^2). UV-Vis measurements were then taken at 30 min intervals. The resulting UV-Vis absorbance measurements (figure 3.12) appear to indicate the decomposition of methylene blue as evidenced by the decrease of the absorbance peak at 650 nm. When the relative decrease in the absorbance of the peak at 650 is plotted as a function of time a linear relationship is observed. This is illustrated in figure 3.13, where the average relative absorbance decrease for three separate samples is plotted as a function of time.

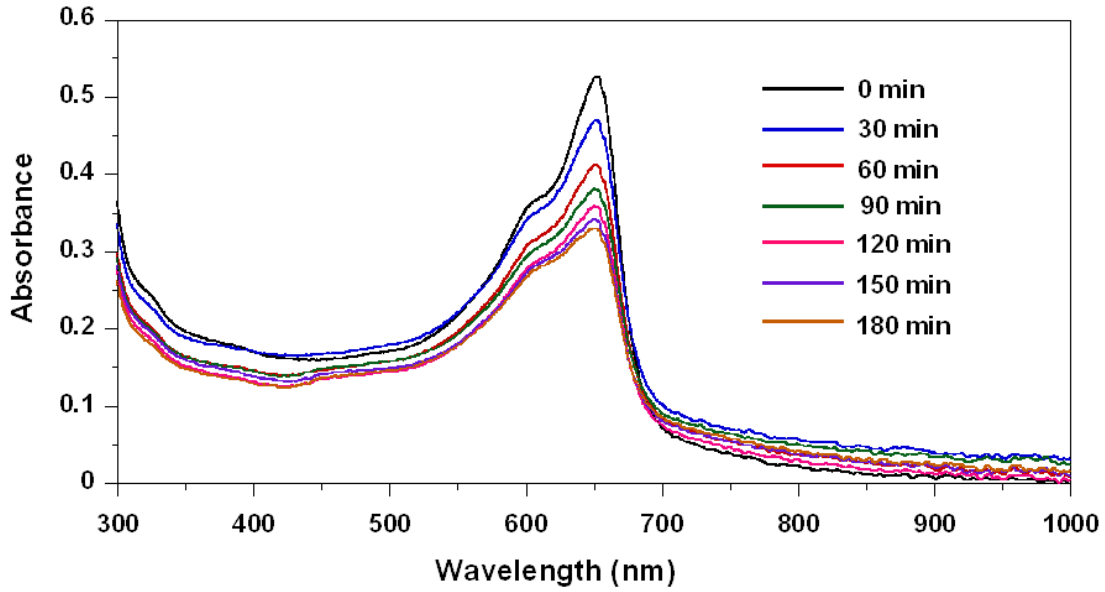

Figure 3.12 UV-Vis Absorbance spectra of Au-Cu_2S in a methylene blue solution illustrating a decrease in the absorbance over time.

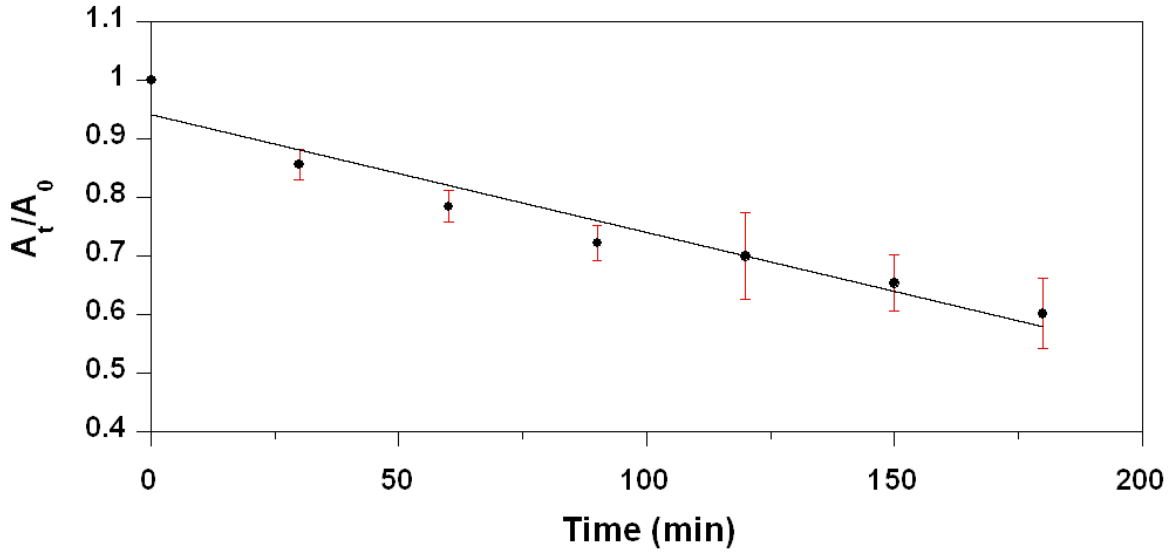

Figure 3.13 Plot of average relative absorbance decrease at 650 nm for three samples as a function of time.

3.4 Conclusions

We have demonstrated that colloidal alloy nanoparticles can serve as compositionally pre-programmed precursors for chemically-triggered phase segregation into colloidal hybrid nanoparticles. The reaction of colloidal AuCu nanoparticles with sulfur in bubbling air produces Au-Cu_2S heterodimers. The availability of a growing library of alloy and intermetallic nanoparticles that could serve as precursors,[12] coupled with other classes of reactions that could induce similar chemically-triggered phase segregation events,[13] suggests that this approach should be general for other materials systems as well. This alternate route to colloidal hybrid nanoparticles could help aid in the rational design and synthesis of a diverse range of new multi-functional nanostructures.

3.5 References

(1) Shi, W.; Zeng, H.; Sahoo, Y.; Ohulchanskyy, T. Y.; Ding, Y.; Wang, Z. L.; Swihart, M.; Prasad, P. N. *Nano Lett*. **2006**, *6*, 875.

(2) Wang, C.; Xu, C.; Zeng, H.; Sun, S. *Adv. Mater*. **2009**, *21*, 3045.

(3) Costi, R.; Saunders, A. E.; Banin, U. *Angew. Chem. Int. Ed*. **2010**, *49*, 4878.

(4) Carbone, L.; Cozzoli, P.D. *Nano Today* **2010**, *5*, 449.

(5) Buck, M. R.; Bondi, J. F.; Schaak, R. E. *Nat. Chem*. **2012**, *4*, 37.

(6) Wang, C.; Daimon, H.; Sun, S. *Nano. Lett.* **2009**, *9*, 1493.

(7) Costi, R.; Saunders, A. E.; Elmalem, E.; Salant, A.; Banin, U. *Nano Lett*. **2008**, *8*, 637.

(8) Cortie, M. B.; McDonagh, A. M. *Chem. Rev.* **2011**, *111*, 3713.

(9) Gu, H.; Yang, Z.; Gao, J.; Chang, C. K.; Xu, B. *J. Am. Chem. Soc.* **2005**, *127*, 34.

(10) Gu, H.; Zheng, R.; Zhang, X.; Xu, B. *J. Am. Chem. Soc.* **2004**, *126*, 5664.

(11) Beveridge, J. S.; Buck, M. R.; Bondi, J. F.; Misra, R.; Schiffer, P.; Schaak, R. E.; Williams, M. E. *Angew. Chem. Int. Ed.* **2011**, *50*, 9875.

(12) Wang, D.; Li, Y. *Adv. Mater.* **2011**, *23*, 1044.

(13) Vasquez, Y.; Henkes, A.E.; Bauer, J.C.; Schaak, R.E. *J. Solid State Chem.* **2008**, *181*, 1509.

(14) Koga, K.; Zubia, D. *J. Phys. Chem. C*. **2008**, *112*, 2079.

(15) Lu, W.; Wang, B.; Zeng, J.; Wang, X.; Zhang, S.; Hou, J. G. *Langmuir*, **2005**, *21*, 3684.

(16) Zhang, Q.; Wang, J.; Jiang, Z.; Guo, Y.-G.; Wan, L.-J.; Xie, Z.;Zheng, L. *J. Mater. Chem*. **2012**, *22*, 1765.

(17) Saruyama, M.; So, Y. G.; Kimoto, K.; Kanemitsu, Y.; Teranishi, T. *J. Am. Chem. Soc.* **2011**, *133*, 17598.

(18) Cokoja, M.; Parala, H.; Birkner, A.; Fischer, R. A.; Margeat, O.; Ciuculescu, D.; Amiens, C.; Chaudret, B.; Falqui, A.; Lecante, P. *Eur. J. Inorg. Chem*. **2010**, *11*, 1599.

(19) Zhou, S.; Yin, H.; Schwartz, V.; Wu, Z.; Mullins, D.; Eichhorn, B.; Overbury, S. H.; Dai, S. *Chem. Phys. Chem*. **2008**, *9*, 2475.

(20) Yu, K.; Wu, Z.; Zhao, Q.; Li, B.; Xie, Y. *J. Phys. Chem. C* **2008**, *112*, 2244.

(21) Dawood, F.; Leonard, B. M.; Schaak, R. E. *Chem. Mater*. **2007**, *19*, 4545.

(22) Odom, T. W.; Nehl, C. L.; *ACS Nano* **2008**, *2*, 612.

(23) Motl, N. E.; Ewussi-Annan, E.; Sines, I. T.; Jensen, L.; Schaak, R. E. *J. Phys. Chem. C* **2010**, *114*, 19263.

(24) Wu, Y.; Wadia, C.; Ma, W.; Sadtler, B.; Alivisatos, A. P. *Nano Lett*. **2008**, *8*, 2551.

(25) Kim, Y.; Park, K. Y.; Jang, D. M.; Song, Y. M.; Kim, H. S.; Cho, Y. J.; Myung, Y.; Park,J. *J. Phys Chem C* **2010**, *114*, 22141.

(26) Chen, W.; Yu, R.; Li, L.; Wang, A.; Peng, Q.; Li, Y. *Angew. Chem. Int. Ed*. **2010**, *49*, 29.

(27) Bjerkelund, E.; Pearson, W. B.; Selte, K.; Kjekshus, A. *Acta Chem. Scand*. **1967**, *21*, 2900.

(28) Sadanaga, R.; Ohmasa, M.; Morimoto, N. *Mineral. J*. **1965**, *4*, 275.

(29) Davey, W. P. *Phys. Rev*. **1925**, *25*, 753.

(30) Zhao, Y.; Pan, H.; Lou, Y.; Qiu, X.; Zhu, J.; Burda, C. *J. Am. Chem. Soc*. **2009**,*131*, 4253.

(31) Kriegel, I.; Jiang, C.; Rodriguez-Fernandez, J.; Schaller, R. D.; Talapin, D. V.; da Como, E.; Feldmann, J. *J. Am. Chem. Soc*. **2012**, *134*, 1583.

Chapter IV
Nanoparticle-Enabled Fabrication of Mesoscale Metallic Components

4.1 Introduction

The development and expansion of microfabrication techniques is becoming a requisite for technological advancement as devices increasingly rely on improvements in the miniaturization and large scale manufacture of various components. Such advances could include the development of highly localized drug delivery systems and mesoscale (i.e., 1 to 1000 micron) surgical instruments for minimally invasive procedures.

One recent microprocessing technique that has been shown to produce components with micro- and nanoscale features for ceramic materials is the lost mold – rapid infiltration forming (LM-RIF) process[1] (figure 4.1). In this process, chemically aided attrition milling (CAAM)[2] is used generate a concentrated suspension of granulated ceramic particles. In this milling method, particles are reduced in size through collisions with each other within a dynamic media. This has the effect of increasing dispersion speed when compared with other milling methods. The resulting suspension is then used to fill photolithographic mold cavities through rapid infiltration forming (RIF). The resulting material then is sintered, which also removes the mold through thermolysis during the firing cycle. The resulting free parts can then be washed off of the substrate for subsequent use.

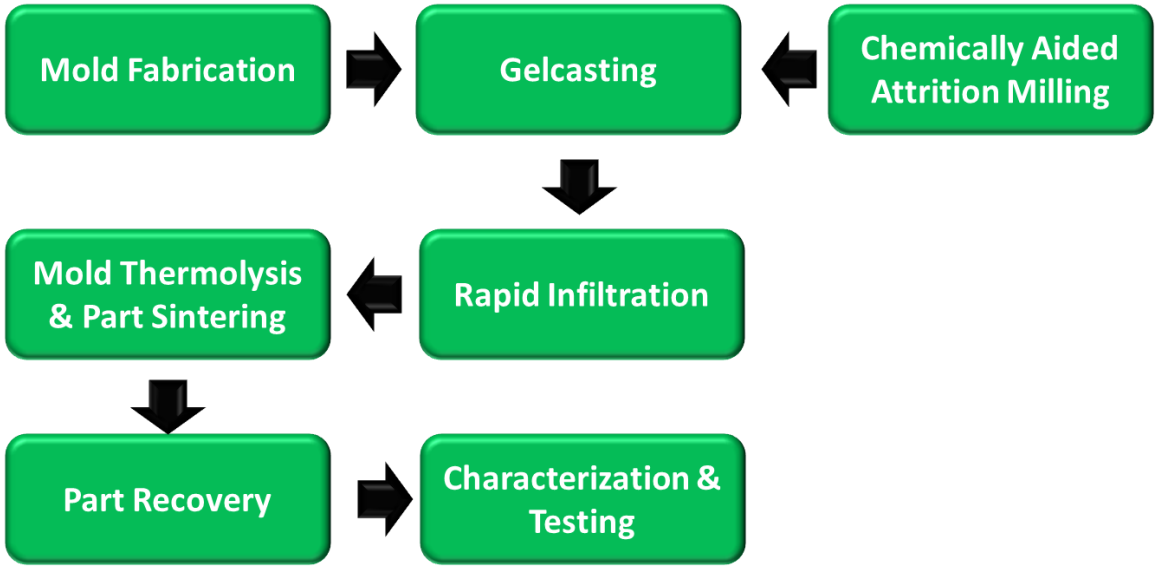

Figure 4.1 A schematic illustrating the lost mold – rapid infiltration forming (LM-RIF) process.

One class of materials that can benefit from the LM-RIF approach to mesoscale part fabrication is that of metal nanoparticles.[3] Utilizing these particles as precursor materials will allow the current LM-RIF process to expand beyond ceramics to include a vast library of unique materials that include non-equilibrium phases[4] and shape memory alloys.[5] The lost mold-rapid infiltration forming (LM-RIF) process requires the use of dispersions of nanoparticulate zirconia with typical concentrations of 45% by volume. This relatively high concentration is required to generate the sufficient viscosity in the dispersion necessary to fill the mold cavity. Unfortunately for most metal nanoparticles, it is difficult to generate the relatively high volumes and concentrations that the LM-RIF process requires. If a solution of gold nanoparticles, for example, were synthesized with the minimum volume and concentration amounts necessary for the LM-RIF process (5mL and 35% by volume, respectively), 48 g of gold nanoparticles would be required.

The relatively high mass required results in the LM-RIF process being both expensive and impractical for most metal nanoparticle systems.

In this chapter we describe the adaptation of LM-RIF process to enable centripetal casting of the metal nanoparticulates based on lower solid content and smaller volumes. We developed the process through four distinct generations, culminating in the fabrication of mesocale parts from 10 nm spherical gold nanoparticles. This work utilized copper and gold nanoparticles as a prototype system. The resulting technique is general and should be applicable to a wide range of inorganic nanoparticles.

4.2 Experimental Details

4.2.1 Materials Used

Hydrogen tetrachloroaurate trihydrate [99.99%, $HAuCl_4 \cdot 3H_2O$], copper (II) acetate [98%, $Cu(OOCCH_3)_2 \cdot H_2O$], tetraethylene glycol [99%, $HO(CH_2CH_2O)_3CH_2CH_2OH$], sodium borohydride [98% $NaBH_4$], cetyltrimethylammonium bromide [98% $((C_{16}H_{33})N(CH_3)_3)Br$], sodium citrate [90.0% $Na_3C_6H_5O_7 \cdot 2H_2O$] and 1-octadecene [tech. 90%, $C_{18}H_{36}$] were purchased from Alfa-Aesar. Oleylamine [tech. 70%, $C_{18}H_{37}N$] and trioctylamine [98%, $C_{24}H_{51}N$] were purchased from Sigma-Aldrich. Poly(vinylpyrrolidone) [MW = 15000] was purchased from Fluka.

4.2.2 Synthesis of Nanoparticles

Copper nanoparticles were synthesized using a modified version of the polyol approach.[6] Specifically, 1.25 g of copper (II) acetate and 400 mg of

poly(vinylpyrrolidone) (MW = 15000) were dissolved in 50 mL of tetraethylene glycol via stirring for 1 h of argon bubbling. The lengthy stir time is necessary to ensure that the copper (II) acetate is completely dissolved. If the synthesis is attempted without argon bubbling, the resulting particles will contain a large amount of oxide impurities. Once the copper (II) acetate was completely dissolved, the temperature was raised under these conditions to 210°C over the course of 90 min. As the temperature was increased, the color of the solution changed from blue to brown, indicating the reduction of Cu^{2+} to Cu^{0}. Once 210°C was reached, the solution was held at this temperature for 15 min and subsequently cooled to room temperature. The particles were then isolated by centrifugation at 12000 rpm and dispersed in ethanol. These particles were used in the fabrication of generation-I parts.

Gold nanoparticles were synthesized in polar media using a borohydride reduction[7] route. 1.00 g of hydrogen tetrachloroaurate trihydrate was dissolved in 100 mL of ethanol along with 5.00 g of poly(vinylpyrrolidone) under vigorous stirring at 40°C. The increased temperature was necessary to ensure complete reagent dissolution. After 30 min at this temperature, the solution was allowed to cool. Once room temperature was reached, 10 mL of a 1.2 M solution of sodium borohydride was added dropwise. In order to ensure the proper reduction rate, the borohydride solution was chilled via ice bath before its addition to the gold solution. As the borohydide was added, the solution color changed from yellow to a deep wine red. This color change[8] indicated the reduction of Au^{3+} to Au^{0}. The resulting nanoparticles were isolated via centrifugation at 12000 rpm and were dispersed in ethanol. These particles were used in the fabrication of generation-I parts.

Gold nanoplates were synthesized using a variation of a previously published method.[9] In this method, two solutions were prepared separately. In the first solution, 2.5 mL of 0.01 M hydrogen tetrachloroaurate trihydrate, 10 mL of 0.015 M CTAB, and 7.5 mL of 18 MΩ nanopure water were heated to 50°C under stirring. The second solution was 30 mL of $3.4x10^{-3}$ M sodium citrate that was heated to 50°C under stirring. Once this temperature was reached, the first solution was injected via syringe into the second solution. Immediately after the injection, the resulting solution was heated to 85°C over 20 min, and was held at this temperature for 15 min. The resulting solution was cooled to room temperature and the particles were isolated via centrifugation at 12000 rpm and were dispersed in ethanol.

Uniform spherical gold nanoparticles were synthesized using a previously published procedure.[10] 1.00 g of $HAuCl_4 \cdot 3H_2O$ was dissolved in 100 mL of 1-octadecene and 100 mL of oleylamine. The solution was then stirred vigorously and heated to 120 °C at a ramp rate of 6.7 °C/min. The solution was then held at this temperature for 45 min and subsequently allowed to cool to room temperature. The resulting Au particles were isolated with centrifugation and washed several times with ethanol and dispersed in hexanes. These particles were later used in the fabrication of generation-II, -III, and -IV parts.

4.2.3 Mold Preparation

Molds were created in a class-10 clean room by spincoating an antireflective coating, Barli-II 90 (Barli-II 90, Clariant Corp., Charlotte, NC), onto an alumina substrate (Kyocera Industrial Ceramics Inc, Somerset, NJ). Two 25-mm-thick layers of SU8-25

photoresist (Microchem Corp., Newton, MA) were then spin-coated onto the substrate. The first layer was exposed without a mask for one minute at 8 mW/cm^2. The second layer was exposed through a filter created from a 100-mm-thick layer of SU8-100 (Microchem Corp., Newton, MA) on a glass mask plate for 120 s at 8 mW/cm^2. All other spin-coating parameters were based on the SU8 manufacturer's recommendations.

4.2.4 Mesoscale Part Fabrication

Generation-I parts were fabricated through modification of the LM-RIF process. Specifically, previously fabricated mold cavities were filled by centripetal casting suspensions of copper nanoparticles or gold nanoparticle aggregates ranging from 100 g/L to 500 g/L at 13500 rpm. This procedure filled the mold cavities and coated the mold with a particulate bed. The mold was then placed into a sealed latex bag and cold isostatically pressed (CIP) at 30 ksi for 30 s to further consolidate the particles. The mold was then thermally treated on a hot plate (up to 300°C) or a furnace (up to 1000°C) to sinter the particles to near theoretical density. This heating also collapses the mold or removes it completely if heated above 600°C, consequently freeing the parts for further study.

In the fabrication of generation-II parts, the spherical gold nanoparticles were first concentrated by centrifugation at 14000 rpm for 30 min. This concentrated solution was then pipetted directly onto the mold which is subsequently centrifuged at 14000 rpm for an additional 30 min. This filled mold was then heat treated at 150°C for 45 min to evaporate residual solvent. The mold was then cold isostatically pressed to 22 ksi to increase particle packing density. The filled mold was then heat treated a second time at

300°C for 45 min. The resulting overburden was chemical mechanically polished off using only a Chem-Pol pad and a 50 nm alumina silica slurry. The mold was then heated in an oven at a ramp rate of 5°C/min to 475°C for 20 min in order to separate the mold from the parts.

Generation-III parts were generated by first diluting an 11 mg/mL dispersion of spherical Au nanoparticles in in hexanes with acetone in a 3:1 ratio. This was done to better facilitate the casting of the particles via centrifugation. The resulting suspension was then added to a centrifuge tube equipped with a mold and a custom designed casting platform. The mold was then filled upon centrifugation at 11000 rpm for 30 min. The resulting supernatant was decanted and the solution was left to dry for 24 hours before characterization.

Generation-IV parts were fabricated in a similar method. In this procedure the 11 mg/mL solution of spherical Au nanoparticles were centrifuged twice in 3:1 acetone : hexanes at 10000 rpm for 5 min in order to concentrate the suspension. The particles were then redispersed in xylenes and 0.14 wt% oleylamine and diluted 1:3 in acetone. The resulting suspension was then added to a centrifuged tube equipped with a mold and a custom designed casting platform. The mold was then filled upon centrifugation at 11000 rpm for 1 hour. The resulting supernatant is decanted and the solution is left to dry for 24 hours before characterization.

4.2.5 Characterization

Transmission electron microscopy (TEM) images were obtained using a JEOL 1200 EX-II microscope operating at an accelerating voltage of 80 kV. Scanning electron

microscopy images were collected using a FEI NanoSEM 630 FE-SEM. Darkfield optical microscopy images were collected with a Nikon Eclipse L200ND. All other optical microscopy images were collected using an Olympus BX60ZVI.

4.2.6 Acknowledgement of Author Contribution

This project was a collaborative effort with Professor James H. Adair, Dr. Nicholas Antolino and Christopher Leh. Copper nanoparticles were synthesized by Nathan Motl. Gold nanoparticles were synthesized by Danielle DeCicco and Nathan Motl. Generation-I copper and gold parts were fabricated by Dr. Nicholas Antolino. Generation-II, -III, and -IV parts were fabricated by Christopher Leh. Scanning electron microscopy (SEM) and optical measurements of generation-I parts were collected by Dr. Nicholas Antolino. SEM and optical measurements of generation-II, -III, and -IV parts were collected by Christopher Leh. Figure 4.6 was prepared by Christopher Leh.

4.3 Results and Discussion

4.3.1 Synthesis of Nanoparticles

Several nanoparticle samples were generated for use in the fabrication of mesoscale components. TEM images of the nanoparticles are shown in figure 4.2. The copper nanoparticles (figure 4.2a) are polydisperse with particle diameters as large as 150 nm. The particles are irregularly-faceted or spherical in shape and tend to form aggregates in solution. The gold nanoparticles synthesized through borohydride reduction in ethanol (figure 4.2b) form aggregated wire-like networks with diameters of approximately 10 nm. The triangular gold nanoplates are shown in figure 4.2c. The plates comprise roughly half of the particles synthesized from this method with the remainder

being a mixture of assorted polyhedra. Although these particles would be suitable for mesoscale part fabrication, we were not able to produce these nanoplates in a quantity suitable for incorporation into mesoscale part fabrication. The spherical monodisperse nanoparticles (figure 4.2d) that are produced are approximately 10 nm in diameter and can be synthesized in large quantities. Additionally these spherical nanoparticles remain colloidaly stable in hexanes for several months without visible signs of aggregation.

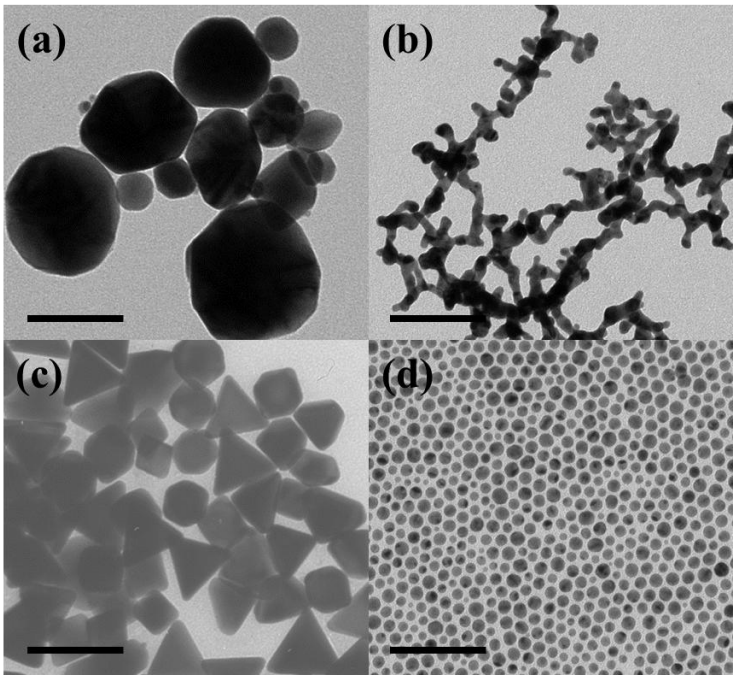

Figure 4.2 TEM images of (a) copper nanoparticles, (b) aggregated gold nanoparticle network, (c) triangular gold nanoplates, and (d) spherical gold nanoparticles. Scale bars are 100 nm.

4.3.2 Generation I

The LM-RIF method was modified with the incorporation of centrifugal casting to consolidate the suspension while simultaneously infiltrating the mold cavity, thereby eliminating the need for suspensions with high solid concentrations. Figure 4.3 demonstrates Cu-parts produced with the LM-RIF process via casting a concentrated

suspension are shown in figure 4.3a-c. Cu-parts produced using centripetal casting with the LM-RIF process are shown in figures 4.3d-g. Figure 4.3a is an image of as-cast Cu-parts while they are still within the mold cavities. The dark rectangular blocks visible in this image are arrays of parts. Each block contains 100 Cu parts, so with 40 blocks in this particular mold, a total of 4,000 parts are contained within the 25 mm x 11 mm area. Figures 4.3b,c show a Cu-part that was heated to 300°C on a hotplate.

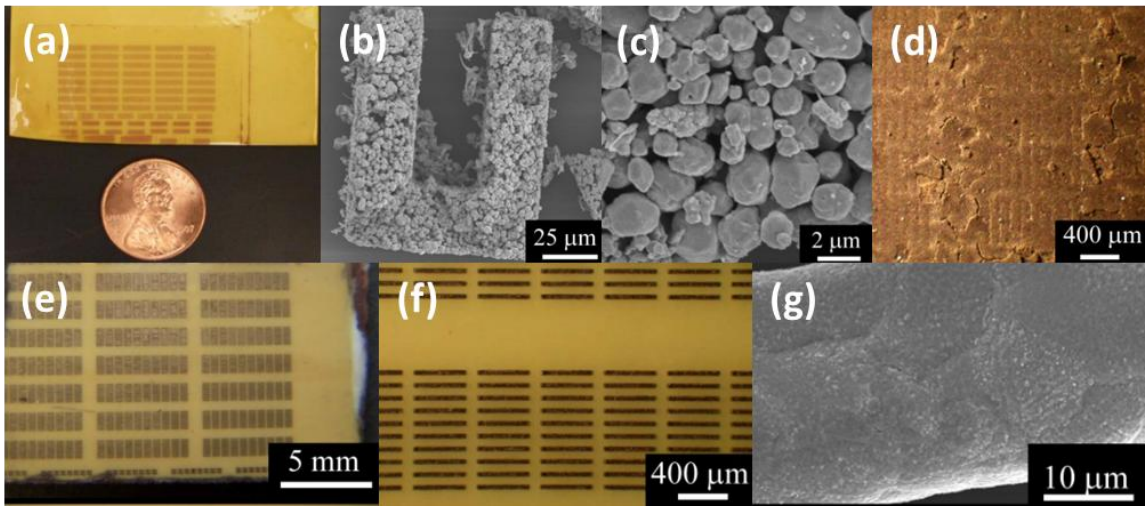

Figure 4.3 Images (a-c) shows copper mesoscale parts that have been formed using a low nanoparticle concentration. Images (d-g) show Cu-parts formed using centrifugal casting with the LM-RIF process. Image (a) illustrates the size of the full mold cavities relative to a penny. Images (b) and (c) illustrate the porosity and large grain sizes due to the low solid concentration in the copper nanoparticle suspension. Image (d) shows mold cavities that are over filled with copper nanoparticles using centripetal casting followed by cold isostatic pressing (CIP). Images (e) and (f) illustrate the neatly arrayed parts once the layer of copper is removed. Image (g) illustrates the dense microstructure after sintering.

The Cu-parts shown did not sinter to a high density due to the relatively low concentration on the nanoparticles used. However, these parts did coarsen into micron-sized disconnected grains. Due to these large grain sizes and poor packing density, cold isostatic pressing (CIP) was introduced in conjunction with centripetal casting. Figure 4.3d shows a mold filled with Cu by centripetal casting followed by CIP. The resulting

bar-shaped parts are aligned vertically in this image and are barely visible under the resulting copper layer. The large cracks that are visible in this image the result of photoresist "springback" after CIP and do not persist to the parts beneath the copper layer. The copper layer can be removed by polishing, revealing the parts in the cavity below (figures 4.3e,f). Figure 4.3g shows a free-standing copper mesoscale bend bar after sintering. This sample has been heated to 1000°C (near the melting point of copper) resulting in grain coarsening.

The generation-I process was also applied to Au nanoparticles (figure 4.2b) in order to bypass material oxidation issues and illustrate the versatility of the modified LM-RIF process. Figure 4.4a shows bar-shaped parts and figure 4.4b shows triangular shaped parts. Figures 4.4c demonstrates that registry on the substrate can be maintained, while figure 4.4d shows that holes can be selectively formed in these parts. These holes tend to crack the entire part due to the stress that results from mold constraints. Fortunately, generating holes with this modified process has not resulted in part cracking. By varying the concentration of the particle solution, it is possible to control the thickness of the particle coating within the mold. Gold deposited onto an alumina substrate with coarse (~10 nm) grains is shown in figures 4.4e,f. The layer of gold deposited into the mold is only a few microns thick, yet conforms to the microstructure of the alumina substrate (figure 4.4f).

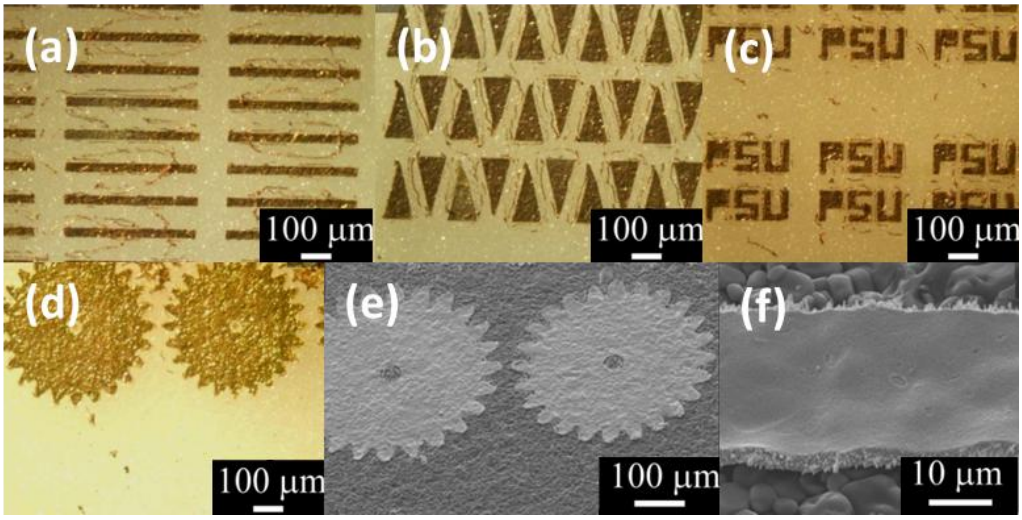

Figure 4.4 All images are of gold parts produced by centripetal casting with the LM-RIF process on top of a polycrystalline alumina substrate. Images (a-d) are optical images in reflection mode. Image (a) shows a mechanical test specimen for strength evaluation. Image (b) shows triangular parts with a ~3 mm radius of curvature. Image (c) demonstrates that the registry of letters is maintained. Image (d) shows gears containing hollow sections. Images (e) and (f) are SEM images of thin parts that can be made to adhere and conform to the substrate. In image (f), the texture of the substrate is reproduced by the gold part.

4.3.3 Generation II

The components in generation II represent the first attempts at casting well dispersed 10 nm spherical gold nanoparticles (figure 4.2d) into the molds. The key modifications present in this method are the pre-concentration of the nanoparticle dispersion and the direct pipetting of the material onto the mold. It is thought that the small particle size and uniform morphology will aid in generating dense particle packing within the resulting components. The materials that result, however, are characterized by exaggerated grains, porosity, cracks, and missing part features (figure 4.5).

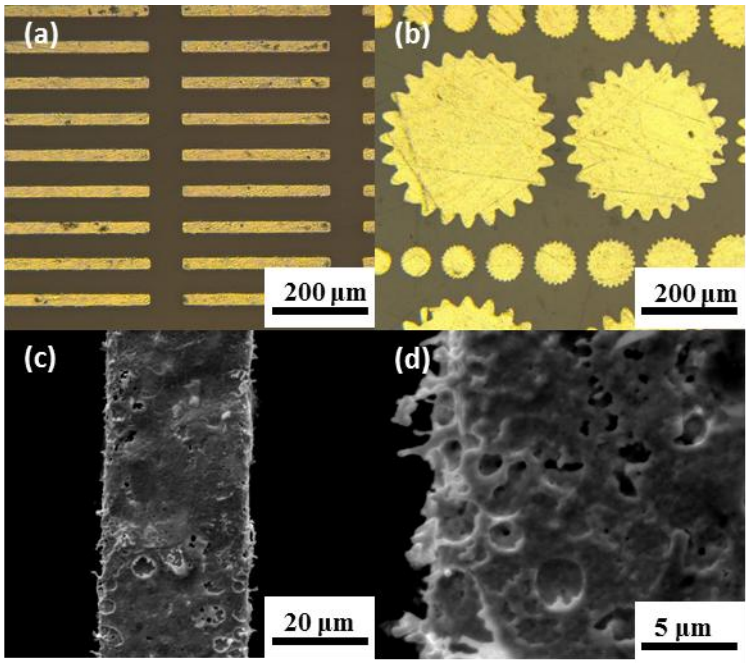

Figure 4.5 Images of generation-II parts produced with 10 nm spherical gold nanoparticles. Images (a) and (b) illustrate the formation of parts with cracks and missing components. SEM images (c) and (d) reveal further defects and porosity.

The defects that result in this process are likely due with difficulty in precipitating the Au nanoparticles from the solution and into the mold. Such a phenomenon would account for the missing components and the irregular packing density observed in figure 4.5. The spheroidal defects that are observed in figures 4.5c,d could indicated rapid loss of the organic surfactant during the sintering process.

4.3.4 Generation III

The modifications present in generation III are focused on maximizing the particle packing density in the casting process. The key development in this iteration is the use of a customized centrifuge tube (figure 4.6) to direct the precipitation of the nanoparticles directly into the mold.

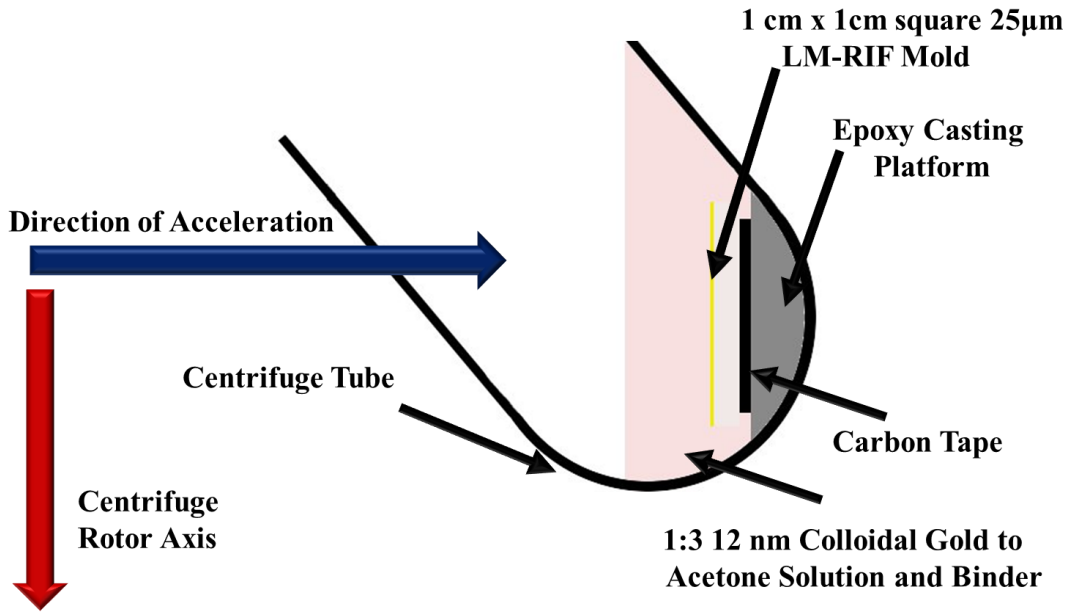

Figure 4.6 Schematic of customized centrifuge tube, illustrating the directed nanoparticle precipitation into the LM-RIF mold**.**

The parts that result from this method are allowed to dry at room temperature, instead of being subjected to heat treatments, in order to examine the mold filling without complications from surfactant loss. Although the filling and packing density is significantly improved in this method, massive anisotropic shrinkage and subsequent cracking is observed. This is illustrated in figure 4.7 where SEM and optical microscopy of the resulting materials are shown.

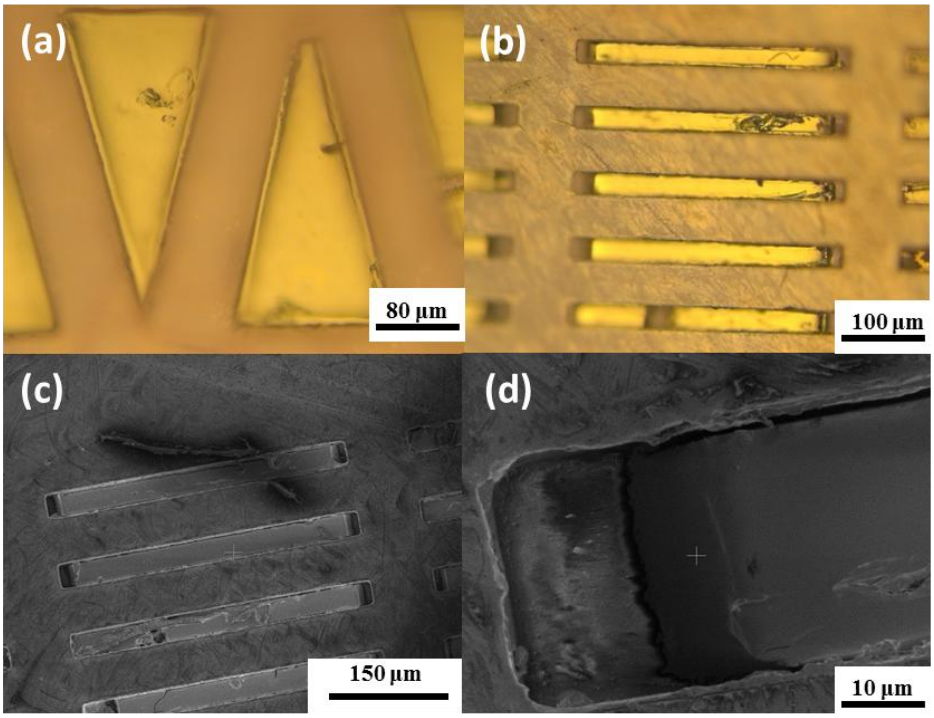

Figure 4.7 Images of generation-III parts fabricated from 10 nm spherical nanoparticles. Images (a) and (b) defects due to shrinkage. SEM images (c) and (d) reveal high packing density and surface uniformity despite edge defects due to shrinkage.

4.3.5 Generation IV

Generation IV addresses the shrinkage present in by incorporating a xylenes and oleylamine mixture as a binder to minimize shrinkage. The LM-RIF mold is also subjected to longer centrifugation times to increase packing density. Although some edge defects are still present in the resulting mesoscale parts (figure 4.8), mold filling is increased and shrinkage is virtually non-existent. There are also large aggregates visible on the mold surface (figure 4.8c,d) which later generations will address through the incorporation of filtration and centrifugation purification into the process.

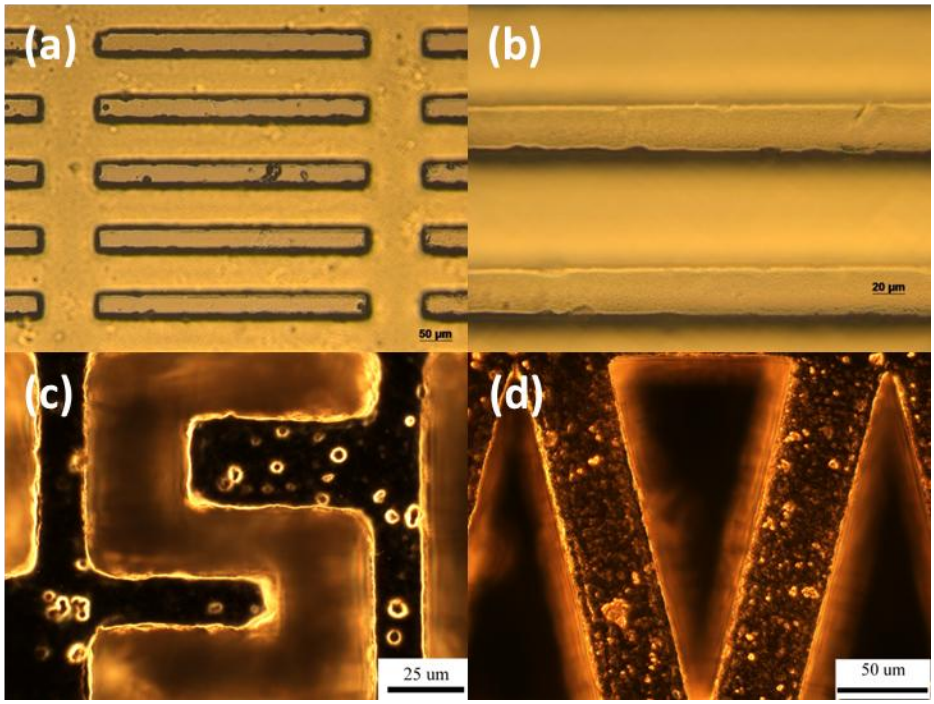

Figure 4.8 Images of generation-IV mesoscale parts fabricated from spherical 10 nm Au nanoparticles. Images (a) and (b) illustrate lack of shrinkage. Images (c) and (d) reveal large aggregates on the mold surface.

4.4 Conclusions

In this chapter we have described the development of the basic colloidal and material processing steps to microfabricate mesoscale components from nanoparticulate Cu and Au. We were able to bypass the LM-RIF requirement of highly concentrated nanoparticle dispersion by incorporating centripetal casting to concentrate the nanoparticles, and cold isostatic pressing to increase the packing density prior to thermal processing. Due to the small particle size, we were able to sinter the parts at relatively low temperature using a hot plate. Although the current generation-IV method has not yet been optimized to produce dense mesoscale components in high yields, the proof of concept demonstrated indicates that dense components can be achieved with further

method refinement and precursor purification to eliminate aggregate impurities. Herein we have demonstrated the ability to generate mesoscale components from metal nanoparticles. This creates the possibility of novel materials based on the ever-increasing array of metallic nanoparticles available.

4.5 References

(1) (a) Antolino, N. E.; Hayes, G.; Kirkpatrick, R.; Muhlstien, C. L.; Frecker, M. I.; Mockensturm, E. M.; Adair, J. H. *J. Am. Ceram. Soc*. **2009**, *92,* S63. (b) Antolino, N. E.; Hayes, G.; Kirkpatrick, R.; Muhlstien, C. L.; Frecker, M. I.; Mockensturm, E. M.; Adair, J. H. *J. Am. Ceram. Soc*. **2009**, *92*, S70.

(2) Adair, J. H.; Shrout, T. R., Messing,G. L.; Mandanas, M. M., Pecora, T. M. "Dynamic control and Enhanced Chemical Milling of Ceramics to Submicron Particle Sizes"; U.S. Patent #6,415,996, 2002.

(3) (a) Wang, D.; Li, Y. *Adv. Mater.* **2011**, *23*, 1044. (b) Schaak, R. E.; Sra, A. K.; Leonard, B. M.; Cable, R. E.; Bauer, J. C.; Han, Y. F.; Means, J.; Teizer, W.; Vasquez, Y.; Funck, E. S. *J. Amer. Chem. Soc.* **2005**, *127*, 3506.

(4) (a) Williams, J. R.; Johnson, D. C. *Inorg. Chem.* **2002**, *41*, 4127. (b) Vasquez, Y.; Henkes, A.E.; Bauer, J.C.; Schaak, R.E. *J. Solid State Chem.* **2008**, *181*, 1509.

(5) Schaefer, Z. L.; Vaughn II, D. D.; Schaak, R. E. *J. Alloys Compd.* **2010**, *490*, 98.

(6) Sra, A. K.; Ewers, T. D.; Schaak, R. E.; *Chem. Mater*. **2005,** *17*, 758.

(7) Pal, U.; Sanchez-Ramirez, J. F.; Liu, H. B.; Medina, A.; Ascencio, J. A. *Appl. Phys. A: Mater. Sci. Process.* **2004**, *79*, 79.

(8) Gole, A.; Murphy, C. J. *Chem. Mater*. **2004**, *16,* 3633.

(9) Huang, W.; Chen, C.; Huang, M. H. *J. Phys Chem*. **2007,** *111*, 2533.

(10) Motl, N. E.; Bondi, J. F.; Schaak, R. E. *Chem. Mater.* **2012**, *24*, 1552.

Chapter V
General Conclusions

The work presented in this dissertation has described our recent contributions to the advancement of complex nanomaterials through the use of gold and gold-copper alloy nanoparticles. We described the uses of gold copper alloy nanoparticles for experimental determination of composition and correlation with theory, as well as their use for the synthesis of Au-Cu_2S heterodimers through phase segregation. Additionally, we discuss the fabrication of mesoscale components from both gold and copper nanoparticles.

Chapter II details the examination of composition-tunable plasmonic nanoparticles. For plasmonic alloy nanoparticles, theoretical modeling and experimental characterization are both central to our capabilities involving predictable synthesis and targeted applications. Highly uniform spherical $Au_{1-x}Cu_x$ alloy nanoparticles were synthesized with compositions ranging from $x = 0$ to 0.5. The particle compositions were analyzed independently using both powder X-ray diffraction (XRD) and energy dispersive X-ray spectroscopy (EDS), which represent two of the most common nanoparticle composition analysis techniques. The plasmon resonance frequencies, determined experimentally for each sample using UV-Vis spectroscopy, red-shift with increasing copper content as expected. These experimentally determined plasmon resonance frequencies were then compared to the values predicted theoretically based upon the XRD and EDS composition measurements. Although EDS and XRD are both found to be acceptable methods for experimentally determining the composition, careful data analysis suggests that XRD composition measurements are more accurate for smaller values of x, whereas EDS measurements are more accurate for larger values of x.

In addition, some discrepancies between the experimentally determined plasmon resonance frequencies and those predicted by theory suggest inaccuracies in using a simple linear mixing rule to determine the dielectric constant of the Au-Cu alloys.

Next we discuss colloidal hybrid nanoparticles, which combine two or more distinct nanoparticle domains fused together through a direct solid-state interface, are typically synthesized by heterogeneously nucleating one material onto the surface of another. An alternative strategy is to pre-program the composition of the metallic components of a desired hybrid nanoparticle into an alloy nanoparticle precursor, then apply a chemical reaction that is selective to only one of the constituent elements. In chapter III, we show that colloidal AuCu nanoparticles react with dissolved sulfur and bubbling oxygen in oleylamine at 172 °C to form phase-segregated colloidal Au-Cu_2S heterodimers. The Au-Cu_2S hybrid nanoparticles, which form in 80% yield, are comprised of 10 ± 2 nm Au domains attached to 7 ± 2 × 4 ± 1 nm domains of hexagonal Ni_2In-type Cu_2S (ß-chalcocite). This alternative route to colloidal hybrid nanoparticles capitalizes on the growing library of available alloy nanoparticles that could serve as precursors and the growing toolbox of nanoparticle transformation reactions that could serve as chemical triggers.

In chapter IV we demonstrate the use of both gold and copper nanoparticles for the fabrication of mesoscale parts. By modifying the existing lost mold – rapid infiltration forming (LM-RIF) process we were able to fabricate several generations of components with nano- and microscale features. This work served as a proof of concept, demonstrating a general technique that could incorporate the vast array of metal nanoparticles available into part fabrication. In addition to the miniaturization of existing

components, this process could potentially lead to such medical advances as microsurgical instruments and localized drug delivery.

The unique characteristics of noble metal nanoparticles have enabled the materials to be utilized in a variety of applications. Many of these applications depend on the ability to predictably modify the properties of these materials through morphological and compositional changes. Low temperature solution methods have been shown to produce colloidally stable nanomaterials with a variety of shapes and compositions. In this dissertation I have described our recent advances in the development and application of complex nanomaterials, specifically gold and gold-copper alloy nanoparticles. The synthetic approaches that are utilized in this dissertation have allowed for control over the composition and morphology of the resulting materials, enabling an in depth examination of the composition and properties of alloy nanoparticles as well as their use for complex nanomaterial synthesis through a phase segregation approach. The materials described in this work serve as model systems by which a series of methodologies can be developed, which should be applicable to a wide range of noble metal and alloy nanoparticle systems. It is the goal of this dissertation to provide future researchers with an enhanced synthetic toolkit as more complex nanomaterials are required for an ever increasing pool of applications.

Vita

Nathan E. Motl

3011 S. Leonard Springs Rd. #55
Bloomington, IN 47403
nmotl25@gmail.com

Education

Ph. D.; Inorganic Chemistry, The Pennsylvania State University, August 2012

B.S., Chemistry, Southern Illinois University, Edwardsville, May 2007

Publications

C. G. Leh, N. E. Motl, N. E. Antolino, R. E. Schaak, J. H. Adair, *Manuscript in Preparation*.

N. E. Motl, J. F. Bondi, R. E. Schaak, *Chem. Mater.* **2012**, *24*, 1552-1554.

N.E. Motl, E. Ewusi-Annan, I. T. Sines, L. Jensen, R. E. Schaak, *J. Phys. Chem. C* **2010**, *114*, 19263-19269.

N. H. Chou, K. C. Oyler, N. E. Motl, R. E. Schaak, *Chem. Mater*. **2009**, *21*, 4105-4107.

Honors and Awards

Graduate Student Chemistry Department Travel Award, The Pennsylvania State University, 2011
Thomas D. Bouman Research Award, Southern Illinois University, 2007
Outstanding Senior Chemistry Student Award Southern Illinois University, 2007
Ik-Ju Kang Student Award in Physics, Southern Illinois University, 2007
ACS Outstanding Junior Chemistry Student Award, Southern Illinois University, 2006
Physics Student Underclassman Award, Southern Illinois University, 2006
Thomas D. Bouman Research Award, Southern Illinois University, 2006
Undergraduate Research Academy Scholar, Southern Illinois University, 2005-2006
Outstanding Student in Chemistry Award: Organic, Southern Illinois University, 2005